PLEASE CITE THIS ARTICLE AS DOI: 10.1063/5.0078985

On the role of bandwidth in pump and seed light waves for stimulated Raman scattering in inhomogeneous plasmas

Mufei Luo,[1, 2, 3, a)] Stefan Hüller,[3] Min Chen,[1, 2] and Zhengming Sheng[1, 2, 4]
[1)] *Key Laboratory for Laser Plasmas (MOE), School of Physics and Astronomy, Shanghai Jiao Tong University, Shanghai, 200240, China*
[2)] *Collaborative Innovation Center of IFSA (CICIFSA), Shanghai Jiao Tong University, Shanghai 200240, China*
[3)] *Centre de Physique Théorique (CPHT), CNRS, Ecole Polytechnique, IP Paris, 91128 Palaiseau Cedex, France*
[4)] *SUPA, Department of Physics, University of Strathclyde, Glasgow G40NG, UK*

The effects of incoherence in the three-wave coupling process of backward stimulated Raman scattering (SRS) in inhomogeneous plasmas are investigated theoretically and numerically via a three-wave coupling model. The impact of the plasma wave nonlinearity is taken into account, namely the effect of trapped electrons via a nonlinear frequency shift of the electron plasma wave. Incoherence in the coupling is introduced in the seed wave and the laser pump wave via bandwidth associated with a Lorentzian power spectrum. It is found that temporal incoherence can suppress the instability as long as the gain associated with spatial amplification in an inhomogeneous plasma ("Rosenbluth gain") is smaller than 2. Otherwise, kinetic effects may destabilize SRS and significantly increase the backscatter level. For the bandwidth effects of the pump laser, a statistical analysis has been performed to examine the real impact of bandwidth. Moreover, a semi-analytical expression of the growth rate in the nonlinear stage is given. By estimating the bandwidth effects, it is found that a broad bandwidth of the pump laser starts to mitigate the scattering provided that the laser beam coherence time τ_c is shorter than γ_0^{-1}, the inverse of the standard SRS growth rate γ_0. However, to obtain effective mitigation, by maintaining SRS in an almost linear stage, it is found that the criterion $\gamma_0\tau_c \leq 0.35$ has to be fulfilled.

I. INTRODUCTION

Temporal and spatial incoherence[1–3] is widely used in laser-plasma interaction experiments for Inertial Confined Fusion(ICF). The goal is to suppress – or at least to mitigate – the onset of parametric instability processes[4–6], including stimulated Raman scattering (SRS), stimulated Brillouin scattering (SBS), and two-plasmon decay (TPD), etc. These instabilities result from the coupling among incident laser beams, scattered light waves, and excited plasma waves. They not only lead to reduced laser energy coupling to fusion targets but also energetic electron production[7,8], both of which are significantly deleterious for the realisation of fusion ignition.

Several smoothing techniques have been developed, such as random phase plates (RPP)[9,10], which introduce spatial incoherence, can considerably suppress hydrodynamic instabilities. Still, they have only a limited effect on parametric instabilities. Spatio-temporal smoothing techniques have been developed by combining the phase modulation in time and space. The most prominent spatiotemporal smoothing techniques are induced spatial incoherence (ISI)[11,12], and smoothing by spectral dispersion (SSD)[13–15]. Mostly SSD has been installed on major laser facilities.

Partly due to technological constraints in the existing laser facilities, the efficiency of these techniques concerning the control of laser-plasma instabilities remains limited and often unsatisfactory to the goal of the experiments. Furthermore, the lack of control of growing plasma waves arising in these instabilities is often responsible for high instability levels. By interrupting the excitation of plasma waves via induced incoherence in time, mitigation of the instabilities may be achieved[16,17]. There is hence a vital need to understand how temporal smoothing techniques can be improved to control better the onset of stimulated scattering instabilities[18].

Usually, the temporal incoherence in laser beams is associated with a single parameter, namely the bandwidth. While the incoherence can be induced in various types[16,19–21]. The adequate bandwidth is directly associated with the laser beam coherence time. The relation between the bandwidth and coherence time could vary depending on the method applied.

In general, it is assumed that the mitigating effect in an instability process is achieved if the coherence time τ_c, is shorter than the growth time of the instability, or the inverse of the homogeneous growth rate γ_0, i.e. (see Ref. 12), $\tau_c < \gamma_0^{-1}$.

However, the instabilities turn easily into a nonlinear regime, for instance, if convective amplification leads to non-negligible plasma wave amplitudes. The latter may lead to the destabilization of an intermediate amplification stage due to nonlinear waves[22,23]. This may eventually alter the impact of spatial and temporal smoothing significantly.

Currently, induced temporal incoherence techniques,

[a)] Electronic mail: mufei.luo@polytechnique.edu

in general, are not conceived to be adjusted due to feedback with upcoming nonlinear processes arising in laser-plasma interaction.

This work studies the effects of temporal incoherence on the three-wave (3-wave) coupling process, particularly on SRS. An incident laser beam is scattered off an electron plasma wave, resulting in a scattered light wave. We concentrate here on backscattering in an inhomogeneous plasma density profile. A nonlinear process from the excitation of trapped particles[24] in the electron plasma wave results in the detuning of the resonant 3-wave coupling.

Our study is based on the well-known one-dimensional model for SRS[25,26]. The low computational expense allows us to identify the key physics via a large number of simulations running with varying incoherence parameters of the incident laser and the plasma. In contrast, numerical simulations in more than one spatial dimension are mostly based on a single or only very few realisations.

This paper is organized as follows. In Sec. II, we introduce the modified 3-wave coupling model for SRS. The statistical properties of the source term are given, which accounts for the thermal noise in plasma. Moreover, the temporal envelope of the pump laser with specific bandwidth is introduced. In Sec. III, we consider different combinations between the choice of laser bandwidth and incoherence in the noise term. The statistical properties and temporal evolution of the scattering are shown. A method to estimate the bandwidth effects is additionally introduced in Sec. IV. Finally, in the concluding Sec. V we discuss further aspects and limitations.

II. THREE-WAVE COUPLING MODEL

Stimulated Raman backscattering can be described by the following system of coupled envelope equations for the pump laser field, the scattered light field, and the longitudinal field of the electron plasma wave (EPW), relevant for an under-dense and warm plasma:

$$\mathcal{L}_0 A_0 = -\frac{e k_L}{4 m_e \omega_0} E_L A_1, \tag{1}$$

$$\mathcal{L}_1 A_1 = \frac{e k_L}{4 m_e \omega_1} E_L^* A_0, \tag{2}$$

$$\mathcal{L}_L E_L = \frac{e k_L}{4 m_e \omega_L} \omega_{pe}^2 A_1^* A_0, \tag{3}$$

where the slowly varying complex envelopes A_0 and A_1 stand for the vector potentials of the pump laser field and scattered light field. In one-dimensional geometry, the differential operators $\mathcal{L}_{0,1}$ describe uni-directional wave propagation for the pump and scattered light, given by $\mathcal{L}_{0,1} \equiv \frac{\partial}{\partial t} + c_{0,1}\frac{\partial}{\partial x}$, where c_0 and c_1 denote the group velocities for the pump and the scattered light, respectively, with opposite signs. $\mathcal{L}_L$ is the differential operator for the EPW, which is associated with a longitudinal electric field E_L. $\omega_{pe} = (n_e e^2/\epsilon_0 m_e)^{1/2}$ is the electron plasma frequency defined in terms of electron density n_e, electron mass m_e, electron charge e, and the vacuum dielectric constant ϵ_0. The matching conditions for 3-wave interaction are given by

$$\boldsymbol{k_0} = \boldsymbol{k_L} + \boldsymbol{k_1} \text{ and } \quad \omega_0 = \omega_L + \omega_1,$$

with $\boldsymbol{k_{0,1,L}}$, $\omega_{0,1,L}$ as the wave vectors and frequencies of the pump laser, scattered light, and EPW, respectively. The differential operator $\mathcal{L}_L$ for the EPW reads $\mathcal{L}_L \equiv \frac{\partial}{\partial t} + c_L\frac{\partial}{\partial x} + \nu_L + i\sigma(x, x_{res}) + i\delta\omega_{\rm nl}$, wherein ν_L denotes the damping rate, $\sigma(x, x_{res})$ takes into account the mismatch around the resonance, at x_{res}, in case of an inhomogeneous plasma density profile, and $\delta\omega_{\rm nl}$ the nonlinear frequency shift due to wave-particle effects. For a given, linear density profile $n_e = n_{e0}\left[1 + (x - x_{res})/L\right]$ with L denoting the density gradient length, we have[5]

$$\sigma(x, x_{res}) = c_L k' x, \tag{4}$$

by taking $x_{res} = 0$, with $k' = \omega_{pe(x=x_{res})}^2/(6 v_{th}^2 L k_L)$ in which $v_{th} = (k_B T_e/m_e)^{1/2}$ denotes the thermal electron speed, k_B the Boltzmann constant, and T_e the electron temperature.

Furthermore, in the kinetic regime[27], in particular for product between the EPW wave number k_L and the Debye length $\lambda_D \equiv v_{th}/\omega_L$ in the range $k_L\lambda_D > 0.25$, wave-particle effects are non-negligible. With increasing plasma wave amplitude, the probability of electrons being trapped in the potential wells of the EPW – running with phase velocity $v_\phi = \omega_L/k_L$ – increases. These trapped electrons create a plateau in the velocity distribution function, reducing the Landau damping and modifying the EPW dispersion. It has been shown, first by the seminal work by Morales and O'Neil[28] and Dewar[29], that this modification can be expressed via an effective, called 'kinetic frequency shift' $\delta\omega_{\rm nl}$ of the EPW that can be used in the envelope wave equation (3). This nonlinear frequency shift $\delta\omega_{\rm nl}$ is proportional to the square root of the EPW amplitude,

$$\delta\omega_{\rm nl} \equiv -\widetilde{\eta}\,|E_L|^{1/2} \text{ with } \widetilde{\eta} = -0.83\omega_L\sqrt{\frac{e}{m_e k_L}\left.\frac{\partial^2 f_0}{\partial v^2}\right|_{v_\phi}} v_\phi^2\ , \tag{5}$$

with f_0 as the Maxwell distribution.

To simplify the analysis, we introduce in what follows the dimensionless variables, time and spatial coordinates are normalized by $1/\omega_0$ and $1/k_0$, respectively. Furthermore, we rewrite Eqs. (1)-(3) in terms of scaled action amplitudes, namely $a_{0,1} \equiv A_{0,1}/A_{00}$, where $A_{00} = (2I_{00}/c\epsilon_0\omega_0^2)^{1/2}$, with I_{00} being the intensity of incident pump laser. The electric field E_L of the EPW is replaced with the normalized density perturbation $n_L = i\delta n_e/n_{e0}$ using $E_L = i(n_e e/\epsilon_0 k_L)(\delta n_e/n_e)$ from Poisson's equation. The system finally reads

$$\hat{\mathcal{L}}_0 a_0 = \frac{\omega_{pe}^2}{4\omega_0^2} n_L a_1, \tag{6}$$

$$\hat{\mathcal{L}}_1 a_1 = -\frac{\omega_{pe}^2}{4\omega_0\omega_1} n_L^* a_0 + S(x_R, t)H(t), \tag{7}$$

$$\hat{\mathcal{L}}_L n_L = -\Gamma_L a_1^* a_0, \tag{8}$$

with

$$\hat{\mathcal{L}}_L = \frac{\partial}{\partial t} + v_L \frac{\partial}{\partial x} + \widetilde{\nu}_L + i v_L k'' x - i\eta\ \omega_L |n_L|^{1/2},$$

v_0, v_1 and v_L are the velocities normalized by the speed of light. The other coefficient result in $k'' = k'/k_0^2$ and $\widetilde{\nu}_L = \nu_L/\omega_0$, with the kinetic factor

$$\eta = (n_e e/k_L \epsilon_0)^{1/2} \widetilde{\eta}/\omega_L. \tag{9}$$

The source term $S(x_R, t)H(t)$ at the boundary $x = x_R$ on the right-hand side of Eq. (7) accounts for the noise of the scattered light and is, therefore, a stochastic function in time, where $H(t)$ denotes the Heaviside function. The statistical properties of the process $S(x_R, t)$ are detailed in the following subsection. The normalized coupling strength in Eq. (8) is given by

$$\Gamma_L = \left(\frac{k_L}{2k_0}\right)^2 \frac{\omega_0}{\omega_L} \left|\frac{eA_{00}}{m_e c}\right|^2 .$$

For the case of a linear density ramp as considered in our simulations, and in the absence of nonlinear terms (no kinetic effects with $\eta = 0$), the solution of the system of coupled envelope equations evolves, after a transient stage, into Rosenbluth's solution[5] that consists essentially in a spatial amplification of the scattered light over the resonance zone. Both the backscattered light and the EPW are amplified in a limited zone in between two points, called 'turning points', from either side of the resonance point with an amplification $\sim \exp(G_R)$, where G_R is the so-called 'Rosenbluth gain,' given by

$$G_R = \pi\gamma_0^2/(v_1 v_L k''), \tag{10}$$

where γ_0 is the standard growth rate of SRS in a homogeneous plasma, given by $\gamma_0 = \omega_0(\omega_{pe}^2\Gamma_L/(4\omega_0\omega_1))^{1/2}$. The gain value G_R is proportional to the intensity of pump laser I_{00}. Note that in most of what follows, the pump laser intensity is therefore quantified – instead of in terms of I_{00} – by the value of G_R

In the presence of kinetic effects with an amplitude-dependent frequency shift, the solution following Rosenbluth's theory can be destabilized in an inhomogeneous plasma, resulting in further growth of the EPW and scattered light. The kinetic frequency shift can compensate for the resonance mismatch from the density gradient (in a particular direction). This phenomenon, called autoresonance (AR) was studied in Refs. 22, 23, 30–32 in one-dimensional (1D) geometry, as well as in 2D in Ref.33.

To quantify the growth and amplification of SRS, an effective gain value G can be defined by the logarithm of the quotient relating the scattered light intensity (if necessary time-averaged) – when exiting the plasma at the left-hand side ($x_L = -L_x/2$) – to its input value at the right-hand side ($x_R = L_x/2$) entrance of the scattered light seed (if necessary time-averaged),

$$G = \ln|\bar{I}_1(x_L)/\bar{I}_1(x_R)|^{1/2} . \tag{11}$$

This effective gain value can evolve in time due to the destabilization from kinetic effects. However, it should not reflect short-term oscillatory and/or stochastic fluctuations so that time averaging may be necessary. For the scattered light intensity at the left boundary $\bar{I}_1(x_L)$ and its input level at the right boundary $\bar{I}_1(x_R)$ this means that for input signals with spectral width, a time averaged value over a sufficiently long time interval T_0 has to be determined, $\bar{I}_1(x_{L,R}) \equiv (1/T_0)\int I_1(t, x_{L,R})dt$.

A. Modelling the noise source

The density and velocity fluctuations[34] of a natural plasma depend on the number of plasma particles and their distribution function, which can be related to average density and temperature. Those fluctuations seed parametric instabilities by coupling with the incident drive laser. Kruer and Rose[35,36] discussed the impact of long-wavelength velocity fluctuations caused during the plasma formation process or by parametric instabilities themselves such that they could act as detuning mechanisms for stimulated Brillouin scattering (SBS). Also, the experimental evidence of plasma fluctuations and their effects on the growth of SBS and SRS has been shown[37]. Recently, in Ref. 38 the sensitivity of SRS to plasma fluctuations in the kinetic regime by the use of particle-in-cell (PIC) simulation was studied. It is proposed that a statistical analysis of backscatter signals with different random seeds could be essential to determine the threshold intensity for inflationary SRS growth.

Alternatively, the effect of the noise source is possible to be modeled by a deterministic boundary value $S(x_R, t)$, to account for the averaged effects of the actual plasma noise[39,40]. The boundary seed $S(t)$ is generated by 'white noise' in time with the following statistical properties:

$$\langle S(t)\rangle = 0, \tag{12}$$

$$\langle S(t)S^*(t^{'})\rangle = \Lambda\delta(t - t^{'}), \tag{13}$$

where Λ is the average intensity of the noise level. For the purpose of numerical simulations, here the stochastic source term $S(t)$ is computed such as to reproduce 'colored noise' with the following statistical properties:

$$\langle S(t)\rangle = 0, \tag{14}$$

$$\langle S(t)S^*(t^{'})\rangle = \frac{\Lambda}{2\tau_1} e^{-|t-t^{'}|/\tau_1}, \tag{15}$$

in which τ_1 is chosen to be always superior to the numerical time step. In the limit where the correlation time τ_1 tends to zero, the source terms reduce to a white noise that satisfies the statistical properties Eqs. (12) and (13) (see the Appendix for the generation of this stochastic source term). Meanwhile, considering the quasi-random feature during one characteristic growth time and the requirement for effective computation, the following condition should be satisfied[40]:

$$\Delta t \ll \tau_1 \ll \tau_\gamma, \tag{16}$$

where Δt is the time step in numerical simulation, and the characteristic growth time τ_γ is defined as $\tau_\gamma = 1/\gamma_0$.

B. Model of broadband pump laser

In a series of work[20,41–43] the incoherent pump laser having a finite frequency bandwidth is generated via a multiple frequency form, here written for the envelope of the pump laser field:

$$a_0(t) = \sum_{j=1}^{N} \hat{a}_j e^{i(-\delta\omega_j t + \phi_j)}, \tag{17}$$

where $N = 4000$ is the number of discrete frequencies used to approximate continuous power spectrum, with $\delta\omega_j = \omega_j - \omega_0$ the randomly taken difference between the frequency of jth plane wave and the central frequency, and ϕ_j the constant phase offset which is randomly selected from a uniform distribution over $[-\pi, \pi)$.

The amplitude of the jth frequency component is

$$\hat{a}_j(\delta\omega_j) = |I_j(\delta\omega_j)/\bar{I}_{00}|^{1/2},$$

with $\sum_{i=1}^{N_\omega} I_j = \bar{I}_{00}$, where $\bar{I}_{00}$ is the time-averaged intensity of the drive laser, and $I(\delta\omega)$ is the power spectrum. The spectrum follows a Lorentzian envelope,

$$I(\delta\omega) = \frac{\bar{I}_{00}}{\pi} \frac{\Delta\omega_0^2/2}{\delta\omega^2 + (\Delta\omega_0/2)^2}, \tag{18}$$

with $\Delta\omega_0$ denoting the frequency range at full width at a half maximum(FWHM). The spectrum is abridged when the amplitude of the spectral intensity attains 0.4% of the peak value. Its range is therefore confined in between the frequencies ω_1 and ω_N, here N =4000 with $\delta\omega_1 = -\delta\omega_N = |\omega_{1,N} - \omega_0|$. The relation between bandwidth $\Delta\omega_0$ and the coherence time is $\tau_c = 2/\Delta\omega_0$. See the Appendix for a discussion and an example of this bandwidth model.

C. Setup of numerical studies

Using a finite difference method we numerically solve the system of partial differential Eqs. (6)-(8) in a single dimension between the boundaries x_L and x_R. The system is seeded by the beating between the two counter-propagating light waves. While the simulations are carried out in dimensionless units, we show the numerical results in units of μm in space and ps in time. Assuming the pump laser wavelength of λ_0 =351nm, an electron temperature of 1KeV, and with a central density of $n_{e0} = 0.05 n_{cr}$. The plasma gradient chosen has a characteristic length $L = 100\mu m$, with a density profile increasing in the pump laser propagation direction, as shown in Fig. 1 (solid red line). Within a simulation window of $250\mu m$, the effective plasma regime is about $150\mu m$, large enough to explore the bandwidth effects. To confine the EPW in the simulation box for avoiding boundary effects, a damping ν_{window} is applied in a buffer zone of the simulation window, ranging from $0.6\omega_{pe}$ at the boundaries of the window to zero across the central plasma region, also shown in Fig. 1 (dashed green line). At the center of plasma, the choice of the plasma parameters results in $k_L(0)\lambda_D(0) = 0.34$. The effective density range in our simulations is $0.0125 n_{cr} < n_e < 0.0875 n_{cr}$, avoiding vicinity to the quarter-critical density with possible onset of absolute instability.

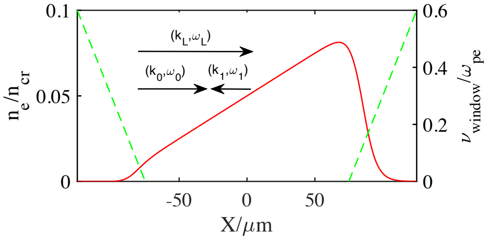

FIG. 1. (Color online) The plasma density n_e with a positive density gradient (solid red line, left vertical axis) and window damping ν_{window} (dashed green line, right vertical axis) taken in the 3-wave coupling system.

The expression Eq. (9) of the kinetic factor η as a function of the spatial coordinate is plotted in Fig. 2 (green line). As shown in the figure, η decreases with increasing density profile (red line), and its value assumes $\eta \approx 0.35$ at the exact resonant point $x_{res} = 0$. Hence, assuming a local value of η would mean that the propagating EPW is subject to decreasing values when running into higher density regions. However, this has been subject to discussion, and as pointed out in Ref. 33, the simple application of Eq. (9) as developed by Morales and O'Neil cannot reproduce PIC simulation results with enough precision. We should keep in mind that the kinetic frequency shift $\eta\omega_L|n_L|^{1/2}$ plays a minor role due to the small amplitude of EPW at the beginning. This term, therefore, mostly matters for sufficiently large EPW amplitude, which is more likely to occur at higher plasma densities, i.e., towards the right-wing of the density profile.

We have performed a comparison between the solutions of the 3-wave coupling equations and kinetic PIC simu-

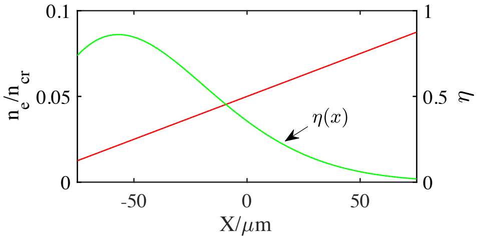

FIG. 2. (Color online) The kinetic factor η (green line, right vertical axis) as a function of space x, along with the effective density profile regime (red line, left vertical axis).

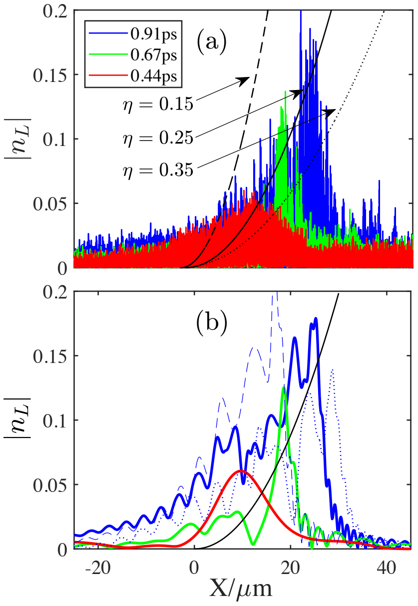

FIG. 3. Spatial profile, in x, of the EPW amplitude taken at three different time instants, t =0.44, 0.67, and 0.91ps, (a) taken from a PIC simulation and (b) taken from solutions of three waves coupling equations, together with the parabola following the solution for AR, Eq. (19), for different values of the parameter η: in (b) bold colored lines correspond to $\eta = 0.25$, while dashed (dotted) correspond to $\eta = 0.15$ ($\eta = 0.35$, respectively). Different colors correspond to different time instants as in (a).

lations, considering the interaction between a relatively high intensity pump laser $I_{00} = 5\times10^{15}\mathrm{W/cm}^2$ and scattered light starting from a coherent seed lightwave signal entering on the right-hand-side of the plasma, with intensity at 1/2000 of the pump intensity. The driven EPW exhibits a significant spatial growth as it propagates from left to right in the profile, as shown in Fig. 3. The PIC simulations in Fig. 3(a) showing the spatial shape of the EPW amplitude $|n_L|$ at different time steps, t =0.44ps, 0.67ps, and 0.91ps, exhibit the propagation of the EPW wavefront advancing further into the profile. As already shown in Refs. 22 and 23, this evolution is a reminiscense of AR, and follows a parabola in x:

$$|n_L| = \left(\frac{v_L k''(x-x_{res})}{\eta\omega_L}\right)^2 . \tag{19}$$

The best agreement between this parabolic shape and the PIC simulation – to follow the EPW wavefront – is obtained for choosing the parameter η =0.25. Similarly, the solutions of 3-wave coupling equations with η =0.25 in Fig. 3 (b) also follow the parabolic shape for t >0.5ps. Due to this good agreement with PIC simulations for the parameter value $\eta = 0.25$, we maintain this choice from now for the rest of the study in this article.

Landau damping ν_L should naturally decrease together with the flattening around the phase velocity v_ϕ in the electron distribution function due to emerging trapped particles. The typical time related to the flattening is the bounce period $\tau_b = 2\pi/\omega_b$, wherein the bounce frequency $\omega_b = |eE_Lk_L/m_e|^{1/2}$ is itself dependent on the EPW amplitude E_L. Certain descriptions given in the literature for the nonlinear evolution of Landau damping have limitations in what concerns their applicability in simulations, either assuming an unrealistic monotonous growth of the EPW amplitude[44,45], or allowing solely a decrease of the local damping value, even for an only transient occurrence of trapped particles.[46]

To allow the Landau damping to locally recover higher values after the departure of trapped particles, such that de-trapping is taken into account, an alternative expression for the nonlinear Landau damping has been proposed in Ref. 33:

$$\frac{\nu_L}{\nu_{L,0}} = \frac{1}{1+(\beta\delta/v_{tr})^4} \quad \text{with} \quad \frac{d\delta^3}{dt} = \frac{\nu_L}{\nu_{L,0}}\sqrt{\frac{\pi}{8}}\,\omega_b v_{tr}^3 \,, \tag{20}$$

where δ accounts for the width of the plateau in the electron distribution function $f(v)$ created by trapped particles[47], $v_{tr} = \omega_b/k_L$ is the trapping velocity. This expression uses the empirical parameter β whose value has been found to yield best agreement with simulations results around $\beta \simeq$1.2. Initially the damping starts with the value of the linear Landau damping coefficient $\nu_{L,0}$ given by

$$\frac{\nu_{L,0}}{\omega_{pe}} = \sqrt{\frac{\pi}{8}}\frac{\omega_{pe}^2\omega_L}{k_L^3v_{th}^3}\exp\left(-\frac{3}{2}-\frac{\omega_{pe}^2}{2k_L^2v_{th}^2}\right), \tag{21}$$

valid for Maxwell distributions. The local value of $\nu_{L,0}$ is plotted in Fig. 4 along the spatial coordinate (green line), simultaneously shown with the positive density profile (red line). The model mentioned above for nonlinear

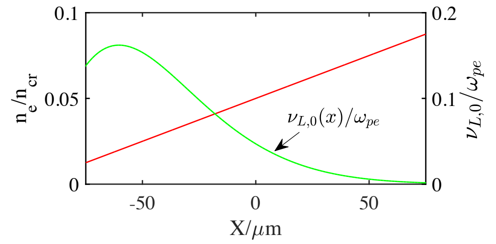

FIG. 4. (Color online) Linear Landau damping $\nu_{L,0}$ (green line, right vertical axis) for $T_e = 1$KeV as a function of the spatial coordinate x, along with the effective density profile (red line, left vertical axis).

Landau damping will be adopted in the Sec. IV. In other sections, we just set $\nu_L = 0$ initially for its rapid descent.

Meanwhile, in the following and in general, we primarily denote the strength of the 3-wave coupling in the respective case via the Rosenbluth gain G_R, a function of the laser intensity. As a guideline for the case of the current configuration (with fixed gradient length and central density value), the pump intensity of $I_{00} = 4 \times 10^{15}\mathrm{W/cm}^2$ corresponds to $G_R = 1$. As reference seed noise level for the incoming scattered light at the boundary, we define $I_{sr} = 2 \times 10^{10}\mathrm{W/cm}^2$.

III. NUMERICAL RESULTS AND ANALYSIS

A. Coherent coupling

One-dimensional wave coupling simulations with a coherent pump laser field entering at $x = x_L$ and a coherent, frequency-matched seed of the scattered light signal incident from the rear at the boundary $x = x_R$ were carried out in Ref. 23. While the emphasis of that work was concentrated on the AR behavior of EPWs, here we focus on the evolution of the backscattering reflectivity in terms of effective gain.

In Fig. 5 we illustrate (a) the instantaneous SRS reflectivity, defined as $R(t) = |I_1(x_L,t)/I_1(x_R,t-L_x/v_1)|$ with $L_x = x_R - x_L$, as well as (b) the effective gain as a function of time for the case of weak initial amplification characterized $G_R = 1$ and by applying different levels of boundary seed: $I_{sr}/5$, I_{sr} and $5I_{sr}$. The instantaneous effective gain is here defined as $G(t) \equiv (1/2)\ln R(t)$, for which no time averaging over a coherence interval is performed.

The time evolution of R and G can be subdivided into three stages: ① within less than one picosecond, the first stage is established such that the scattered light signal is amplified from the seed level to a level corresponding to Rosenbluth gain, the effective gain $G^{(1)}$ is hence $G^{(1)} \simeq G_R$. Up to this stage, kinetic effects are not remarkable but may emerge according to the amplitude of the EPW, giving rise to trapped particle generation. The latter initiates stage ② with the onset of AR in an inhomogeneous plasma profile increasing in density in the direction of the propagating EPW. The solution described by Rosenbluth gain is then destabilized because kinetic effects compensate for the resonance mismatch from the density gradient. The EPW, and consequently the SRS reflectivity, start to increase from the level attained in stage ① . The third stage ③ is characterized by the limit of the AR solution, not allowing the EPW to grow beyond an upper limit (see Ref. 23). Then the evolution of R and G both exhibit violent non-stationary oscillations, which is particularly pronounced for higher seed levels as shown in Fig. 5. By inspection, R may reach several percent in this stage, here $2 \sim 3\%$, similar to PIC simulation results reported in Ref. 33 with the reflectivity of 4%. Pump depletion may come into play at this level, impacting the time evolution.

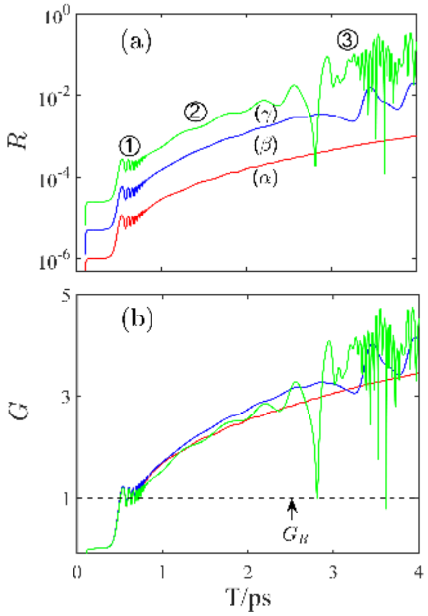

FIG. 5. (a) Instantaneous reflectivity R versus time for different seed intensities: (α): $I_{\mathrm{sr}}/5$, (β): I_{sr}, and (γ): $5I_{sr}$. Curve γ presents the three amplification stages: ① corresponds to fast growth up to 0.5ps and stabilization (Rosenbluth amplification); ② exhibits the destabilization of kinetic effects, the weak nonlinear stage of AR; ③ SRS is further destabilized by the kinetic effects after upper limit of AR is reached, resulting in the further amplification and modulation; (b) Instantaneous amplification factor $G(t)$ for these three different seed intensities.

B. Large bandwidth scattered light seed

We now consider incoherent noise with large bandwidth imposed to seed the incoming scattered light signal at the right-hand-side boundary. The goal is to excite SRS all over in the density profile and not just at a reference density. Note that in this subsection, a coherent pump wave is considered. For an adequate choice, SRS can be resonant everywhere in the plasma and the EPW should be driven at almost all possible modes with $\omega_L \approx \omega_L(0) \pm \Delta\omega_{pe}$, where $\Delta\omega_{pe} = \omega_{pe}(x_R) - \omega_{pe}(x_L)$ is the spectral width of the EPW in the profile. The numerical time step Δt has to be adequately chosen such that the condition Eq. (16) is fulfilled. With the choice

$$\Delta t/\tau_1 = \tau_1/\tau_\gamma \ll 1, \tag{22}$$

one can fulfill also the criterion to numerically solve the Langevin equation (A1). Based on the above argument, we use $\tau_1 = 6\omega_0^{-1} \simeq 1.34\omega_p^{-1}$. Consequently the criterion for the time step is related to the SRS growth rate, $\Delta t = \gamma_0\tau_1^2 \sim \sqrt{G_R}$. For $G_R > 2$ the criterion for the time step is weakly dependent on G_R so that an appropriate choice results in $\Delta t = 0.2\omega_0^{-1}$.

The noise level is taken at the reference intensity I_{sr} as defined above. Using a pseudo-random number generator (PRNG) to generate the boundary noise, for each choice of simulation parameters, 40 realisations of the seed signal are carried out. This allows us to determine the sensitivity of SRS on boundary noise fluctuations, by computing the mean (expectation) value $\langle\bar G\rangle$ and the standard deviation $\sigma(\bar G)$ via an ensemble average over $i = 1 \dots M$ (here M =40) realisations of the effective gain $\bar G$ through SRS, defined as

$$\langle\bar G\rangle = \frac{1}{M}\sum_{i=1}^{M}\bar G\ , \quad \sigma^2(\bar G) = \frac{1}{M}\sum_{i=1}^{M}(\bar G_i - \langle\bar G\rangle)^2. \tag{23}$$

Herein $\bar G(t)_i$ is already a time-averaged value of the amplification gain, due to the usually broad bandwidth of the scattered light seed. Its values is taken over a time interval T_0 following the description of Eq. (11), namely

$$\bar G(t)_i = \frac{1}{2}\ln\left|\frac{\int_{t-T_0/2}^{t+T_0/2} I_1(x_L,t)dt}{\int_{t-T_0/2}^{t+T_0/2} I_1(x_R,t-L_x/v_1)dt}\right|. \tag{24}$$

T_0 has to be chosen with care: it should be long enough to cover the broad bandwidth properties of the scattered light. At the same time, the temporal-evolution characteristics of $\bar G(t)_i$ during the nonlinear stage should also be kept to make $\gamma_k T_0 < 1$ (where γ_k is the growth rate in the nonlinear stage, discussed in Sec. III C). Here, we have taken $T_0 = 0.15$ps$\simeq 135\tau_1$.

The SRS amplification starting from the boundary noise is hence represented by the effective gain $\bar G$ as a function of the Rosenbluth gain G_R, as plotted in Fig. 6. The red circular and blue diamond markers show the simulation results at time t =1ps and 2ps, respectively. For orientation, we also show $\bar G = G_R$, being expected without destabilization, which proves to hold in stage ①. For the regime of low G_R values, $G_R < 1.75$, this suggests that kinetic effects remain unimportant when a large bandwidth seed is applied. The latter is different from the above-shown case when applying a coherent seed in Sec. III A. For the regime of higher Rosenbluth gain values, above $G_R \sim 2$, the measured $\bar G$ values in simulations exceed Rosenbluth's prediction by a factor between one and three, until $G_R \simeq 7$. The onset of saturation due to pump depletion is seen from $G_R > 3$ dependent on the chosen noise seed level. The results of the numerical simulations show that the effective gain $\bar G$ starts deviating from $\bar G = G_R$ in the interval $G_R = 1.75 \sim 2$, above which SRS will be clearly destabilized due to kinetic effects.

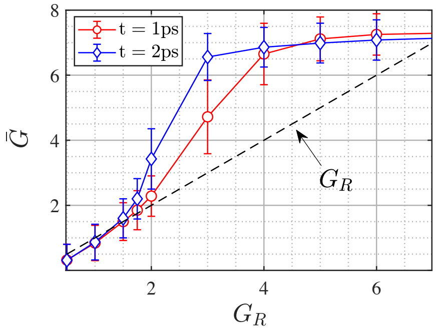

FIG. 6. Effective gain $\bar G$ of SRS backscatter as a function of the Rosenbluth gain G_R (expected without SRS destabilization), here, in contrast to Fig. 5, for the case with an incoherent, large bandwidth seed for the incoming scattered light. Black dashed line: $\bar G = G_R$ as guide line, red circular and blue diamond markers show simulation data at times t =1ps and 2ps, respectively, with error bars from standard deviation.

Furthermore, the standard deviation in $\bar G$ computed from 40 realisations is also shown via error bars in Fig. 6. It proves to be the largest for $G_R = 3$, where also the slope of the curve $\bar G(G_R)$ is steep. The large error bars indicate that in this regime of G_R, the destabilization of SRS expressed via the effective gain is more sensitive to the seed signal. Note that in PIC simulations[38], the largest standard deviation on the effective gain was observed already in the interval $G_R \simeq 1.8 \dots 2.2$, which is most probably since PIC simulations start from a high initial noise level, higher than natural noise and/or higher than the noise level used in our wave-coupling simulations. Consequently, in PIC simulations, EPWs are driven to higher amplitudes with an earlier onset of kinetic effects, compared to simulations allowing for low noise levels.

To relate the density perturbation n_L of EPWs with

G_R as the principal parameter, we can derive the following simple model. According to Eq. (8) by ignoring the damping term in $\hat{L}_L n_L = -\Gamma_L a_1^* a_0$ and assuming a small G_R value, the scattering reaches a stabilization rapidly within a sub-picosecond interval, described by the stationary limit of Eq. (8),

$$\left(v_L \frac{\partial}{\partial x} + i v_L k'' x - i\eta\omega_L |n_L|^{1/2}\right) n_L = -\Gamma_L a_1^* a_0 \ .$$

For small values of G_R, the incoherence in the noise affects mostly the balance between the terms $i v_L k'' x n_L$ and $-i\eta\omega_L |n_L|^{1/2} n_L$ allowing us to drop $\partial_x n_L \to 0$. In addition, each spectral mode contained in the broadband noise source has a different resonance position x_{res} concerning the mismatch term $v_L k''(x - x_{res})$. Following Rosenbluth in using the "turning point" position $x_t = 2\gamma_0/(k''|v_L v_1|^{1/2})$, known as the distance from resonance at which the solution changes from being growing to oscillatory, one can write by taking the absolute value:

$$\left(v_L k'' x_t - \eta\omega_L |n_L|^{1/2}\right) |n_L| = \Gamma_L |S| e^{G_{\rm R}}, \qquad (25)$$

for which in $a_0 a_1^*$, the pump amplitude a_0 has been replaced by unity by ignoring pump depletion and a_1 by $S\exp(G_R)$.

For a selected realisation (which always starts from the same initial PRNG seed), we have performed simulations for different G_R values. The corresponding simulation results are shown in Fig. 7. The density perturbations $|n_L|$ at t =1ps seen in the simulations and depicted in Fig. 7(a) are compared with the solution for $|n_L|$ by numerically solving Eq. (25). The dashed lines indicate these values. They show a good agreement with the peak density perturbations seen in the simulations for $G_R = 0.5$ or 1. This suggests that the length of resonant growth is short, as it is supposed to be above. The length of resonant growth can be associated with the width of the phase-locked zones in space, which arises for $\sin(\phi) \simeq -1$, for the relative phase[48,49] $\phi = \phi_0 - \phi_1 - \phi_L$, between the phases $\phi_{0,1,L}$ of the complex field envelopes of the pump wave, scattered light, and EPW, respectively[22,23,50,51]. Inspecting the spatial behaviour of $\sin(\phi)$ in Fig. 7(b), one cannot find apparent extended phase-locked zones for the cases in (b.1) and (b.2) corresponding to the low G_R values. Kinetic effects prove to be negligible here and can therefore not destabilize SRS. The seen behavior, in the absence of non-negligible kinetic effects, shows therefore an amplification according to Rosenbluth's solution. Beyond stage ①, no further growth of the amplification beyond gain values of G_R is seen in Fig. 7(c). In contrast to this, for $G_R = 2$, see Fig. 7(a.3), an almost 10× higher EPW peak amplitude is observed, together with extended phase-locked zones over $\sim 30\mu$m, see Fig. 7(b.3). The latter results in a discrepancy between the numerical evolution of $|n_L|$ and the one described by the solution to Eq. (25). For the case with high EPW amplitudes and extended phase locking, the assumption of small amplitude modification in n_L, as made to get Eq. (25), cannot be maintained. Hence, the kinetic effects lead to the further growth of the effective gain $\bar{G}$ beyond stage ①, see the green curve in Fig. 7(c).

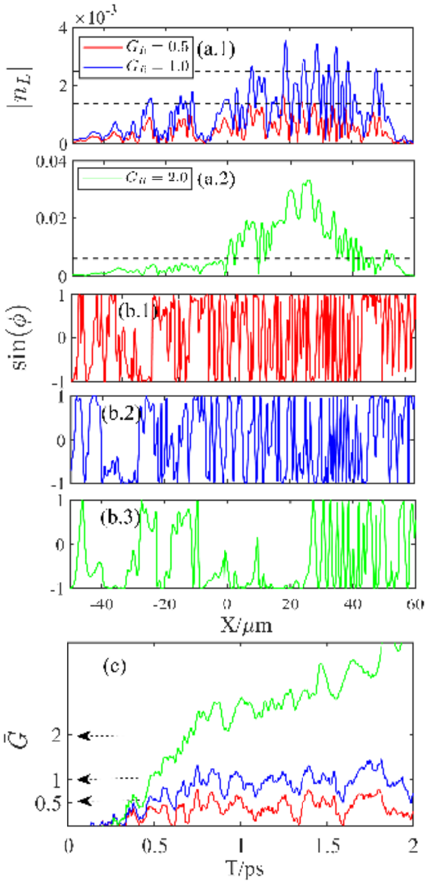

FIG. 7. Red, blue, and green lines represent the cases with $G_{\rm R} = 0.5$, 1 and 2, respectively. Shown are in (a) the density perturbations $|n_L|$ as a function of space at t =1ps. The horizontal black dashed lines indicate the solution to Eq. (25); in (b) $\sin\phi$ of the relative phase $\phi = \phi_0 - \phi_1 - \phi_L$ as a function of x at t =1ps; in (c) the instantaneous effective gain $\bar{G}$ value defined in Eq.(24) as a function of time in ps. All simulation results shown are from a single realisation.

C. Effects of bandwidth in the pump laser on SRS

To discuss the bandwidth effects of the pump laser field, we first neglect the incoherence of the incoming scattered light seed, namely $\tau_1 \to \infty$. In the first step, we choose the pump laser intensity such that the Rosenbluth gain is $G_R = 1$, together with the reference seed level. Higher G_R values are discussed later on.

1. Revisit bandwidth effects on linear convective SRS

In the regime of linear growth, when nonlinear kinetic effects have not yet developed, Guzdar *et al.*[52] showed that convective SRS is insensitive to bandwidth when $\gamma_0\tau_c \ll 1$ because the bandwidth weakens the local growth but broadens the resonance region. While for $\gamma_0\tau_c > 1$, there is a statistical enhancement in the amplification gain.

Theoretically, an incoherent laser pulse with a continuous Lorentzian spectrum has the correlation function of $C_0(\tau) = \exp(-|\tau|/\tau_c)$ with $\tau_c = 2/\Delta\omega_0$. In practice, we apply the bandwidth model Eq. (17) in which the spectrum is composed of many monochromatic modes with frequency difference $\delta\omega_j$, both $\delta\omega_j$ and the phase offset ϕ_j of each mode are taken randomly. Introducing randomness creates the temporally varying laser pulse profile, leading to a deformation of the correlation function, which indirectly impacts the amplification.

Based on a series of pump laser input signals corresponding to different realisations, while conserving the bandwidth parameter value $\Delta\omega_0$, the resulting correlation functions are computed and represented by different color lines in Fig. 8(a). The computed correlation functions vary around the analytically obtained function, also included in the figure (marked by the black dashed line). These laser pump waves from numerous realisations interact with the seed light to excite SRS.

For the case of G_R =1, the values of $\bar{G}$, as defined in Eq. (24) (with a time average over intervals of 0.15ps), and recorded from 40 realisations are represented via a histogram in Fig. 8(b). Each vertical line corresponds to a realisation with its amplification value $\bar{G}$. The cumulative count, being the complementary distribution (CDF) $F_c(\bar{G})$ × the number of realisations M =40, starts with i =1 from the highest towards $i = M = 40$ for the lowest value of $\bar{G}$. It is important to note that although most of the recorded effective gain $\bar{G}$ values are distributed around G_R, a few are considerably higher than G_R. This means that several of these realisations lead to undesirably high SRS amplification: there are about as many realisations counted in the interval $\bar{G}$ >1.8 as in the interval of low values $\bar{G}$ <0.8. Consequently, if the percentage of realisations that lead to significant SRS growth for the chosen bandwidth is non-negligible, the objective to suppress SRS would fail.

For this reason, our following study is focused on the quantification and modeling of the bandwidth regime for which undesirable and detrimental SRS growth could occur. The detail of the bandwidth model that leads to high values of $\bar{G}$ is discussed in the following.

On the basis of numerical simulations with 40 realisations, Table I shows $\langle\langle\bar{G}\rangle\rangle$, as defined below, as well as $\langle\bar{G}\rangle$ and the standard deviation $\sigma(\bar{G})$, as defined by Eqs. (23) as a function of the bandwidth $\Delta\omega_0/\omega_0$, ranging between 0.2% and 8%, or correspondingly of $\gamma_0\tau_c$, ranging between 4 and 0.1, respectively. The relevant gain value, $\langle\langle\bar{G}\rangle\rangle$, to compare the amplification with experimental data can be defined via[52]

$$e^{\langle\langle\bar{G}\rangle\rangle} = \frac{1}{M}\sum_{i=1}^{M} e^{\bar{G}_i} = \int P(\bar{G})e^{\bar{G}}d\bar{G} \ , \qquad (26)$$

using $P(\bar{G})$ as the probability density (PDF) for $\bar{G}$. Note that the gain values defined by $\langle\langle\bar{G}\rangle\rangle$ are systematically greater than the standard expectation value $\langle\bar{G}\rangle$, as seen in Table I. This is because[52,53] the expectation value $\langle f(\bar{G})\rangle$ defined by $\sum_i^M f(\bar{G}_i)/M$ yields $\langle f(\bar{G})\rangle \geq f(\langle\bar{G}\rangle)$ for the case of the exponential function $f(\bar{G}) = \exp(\bar{G})$, with $f''(\bar{G}) > 0$.

It is found that, with respect to the case of a coherent pump wave, $\Delta\omega_0$=0, the effective gain values $\langle\langle\bar{G}\rangle\rangle$ and $\langle\bar{G}\rangle$ increase slightly as the bandwidth $\Delta\omega_0$ is increased. The values reach a maximum around $\gamma_0\tau_c = 1$ and then decrease successively for higher bandwidth values. The standard deviation of the effective gain, $\sigma(\bar{G})$, decreases with increasing bandwidth. In the limit of large $\Delta\omega_0$ values, where $\gamma_0\tau_c \ll 1$, the value of $\langle\bar{G}\rangle$ be-

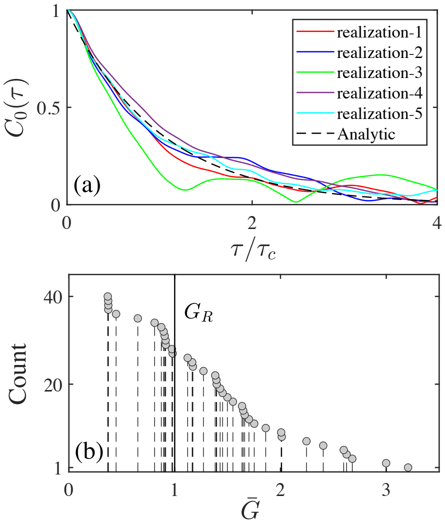

FIG. 8. (a) Correlation functions $C_0(\tau)$ of five signals, which are calculated by use of five different initial PRNG seeds to generate five trains of the pump laser with the same bandwidth. The analytical one is given by the black dashed line. (b) Histogram, i.e. cumulative count, with $i = MF_c(\bar{G}_i)$, $i = 1\ldots M$, of the effective gain values $\bar{G}$ determined from simulations based on M =40 realisations, sorted from the highest, $\bar{G}_1$ ≃3.2, towards the lowest registered value, $\bar{G}_{40}$ ≃0.4. F_c stands for the complementary distribution function (CDF).

comes almost independent of the bandwidth, as can be see from the data for $\Delta\omega_0/\omega_0 \geq 4\%$, for which the variation among them proves to be very small. This is due to the fact that the local growth rate $\gamma(\tau_I)$ is weakened while the resonance region is broadened or/and the interaction time τ_I is lengthened. These two effects result in almost bandwidth-independent values of $\langle\bar{G}\rangle$. This has been described in Ref. 52, by characterizing bandwidth effects via the local growth rate and the interaction time, which reads then:

$$\gamma(\tau_I) = \frac{2\gamma_0^2}{\Delta\omega_0} \quad \text{with} \quad \tau_I = \frac{\pi\Delta\omega_0}{2v_1 v_l k'} \, . \tag{27}$$

The effective gain $\bar{G}$ can be approximated by

$$\bar{G} \approx \int_0^{\tau_I} \gamma(\tau_I) d\tau = \frac{\gamma_0^2 \pi}{v_1 c_l k'}, \tag{28}$$

corresponding to $\bar{G}=G_R$ from Eq. (10) with Eqs. (27).

TABLE I. Average amplification in terms of the effective gain $\langle\langle\bar{G}\rangle\rangle$, from Eq. (26), as well as $\langle\bar{G}\rangle$ from Eq. (23) and its standard deviation $\sigma(\bar{G})$ for different bandwidth values $\Delta\omega_0$ or $\gamma_0\tau_c$ within linear growth. All simulation data are based on 40 realisations.

$\Delta\omega_0/\omega_0$	$\gamma_0\tau_c$	$\langle\langle\bar{G}\rangle\rangle$	$\langle\bar{G}\rangle$	$\sigma(\bar{G})$
0.2%	4.0	2.06	1.12	0.87
0.4%	2.0	1.79	1.15	0.83
0.8%	1.0	2.18	1.37	0.81
1.6%	0.5	1.76	1.30	0.75
2.0%	0.4	1.68	1.31	0.72
4.0%	0.2	1.67	1.14	0.65
6.0%	0.13	1.38	1.09	0.55
8.0%	0.1	1.26	1.07	0.51

To establish a distribution from the data set $\bar{g}(t)$ for $\bar{G}$, we gather $\bar{G}$ both over a time interval and from $i = 1\ldots40$ realisations. The data set is defined as

$$\bar{g}(t) = \bar{G}(t - \bar{T}_0/2 + j\delta T)_i \quad j=1\ldots N_t, i=1\ldots40 \, , \tag{29}$$

with i as the index for the realization and $N_t \equiv \bar{T}_0/\delta T+1$ the number of steps to cover the interval $\bar{T}_0$, which equals to T_0 as mentioned in Eq. (24). With the temporal resolution $\delta T = 7 \times \Delta t \simeq 0.25$fs chosen to record the data, we have $N_t \equiv \bar{T}_0/\delta T+1$=601 data in time for each time t and realization. With this choice, the temporal-evolution features of the distribution are conserved. In total, this yields a data set of $601 \times 40 = 24040$ values to establish the distribution. For the data shown in Fig. 9(a), we have performed a statistical analysis of the elements $\bar{G}$ in $\bar{g}$, which shows first the probability density $P(\bar{G})$ corresponding to the different $\gamma_0\tau_c$ values in the regime of linear growth when kinetic effects are still negligible. Note that the recording time for each set of $\bar{g}$ is adapted to the different bandwidth values, according to the linear growth time τ_I in Eq. (27) for each case. For $\gamma_0\tau_c \leq 1$, where $\tau_c \leq \tau_I$ according to Eq. (27), $P(\bar{G})$ exhibits a distribution peaked around $\bar{G} = G_R$, here $G_R = 1$, with a tendency to narrow with increasing bandwidth. This is expected because the interaction with the pump pulse train goes through numerous different random intensity values during one growth cycle. Consequently, $\bar{G}$ can be considered a sum of independent random numbers, and $P(\bar{G})$ approaches a normal distribution by the central limit theorem.

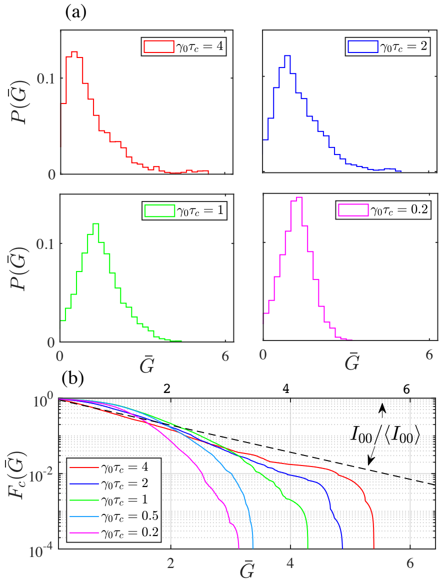

FIG. 9. Probability density function $P(\bar{G})$ (a) and complementary distribution function $F_c(\bar{G})$ (b) for different values of $\gamma_0\tau_c$ in the linear growth regime, disregarding kinetic effects. $P(\bar{G})$ is close to a normal distribution for $\gamma_0\tau_c < 1$, while it results in a mostly exponential dependence on $\bar{G}$ for $\gamma_0\tau_c \geq 1$, and its $F_c(\bar{G})$ has the similar tendency with the complementary distribution function of the instantaneous pump intensity (the black dashed line in (b)).

For small bandwidth, however, i.e. $\gamma_0\tau_c > 1$, having $\tau_c > \tau_I$, the saturation of $\bar{G}$ is reached within τ_c, then $\bar{G}$ adiabatically follows the intensity variation of the pump laser. Therefore $P(\bar{G})$ follows an almost exponential decrease with, however, a long tail. This tail may continue up to high $\bar{G}$ values, which are undesirable, despite their low probability.

The integration of $P(\bar{G})$ from high to low $\bar{G}$ values yields the complementary probability distribution function (CDF) defined as $F_c(\bar{G}) = 1 - \int_0^{\bar{G}} P(\bar{G}')d\bar{G}'$, having $F_c(0) = 1$ and $F_c(+\infty) = 0$. As shown in Fig. 9(b), the CDF $F_c(\bar{G})$ with $\gamma_0\tau_c > 1$ closely follows the CDF of the instantaneous intensity in the pump laser, marked by the black dashed line, except for a cutoff at high $\bar{G}$ values. This cutoff results from the probability of instantaneous high-intensity being too small to participate in the interaction. Another simulation has been performed with a much lower seed-light level, confirming that pump depletion plays a minor role in the cutoff here.

For an ideal adiabatical evolution of $\bar{G}$ with the laser intensity variation, one can calculate $\langle\bar{G}\rangle$ as

$$\langle\bar{G}\rangle = \int_0^{\bar{G}_{\rm cutoff}} \bar{G}e^{-\bar{G}}d\bar{G} \approx 1 \ ,$$

which means $\bar{G} \simeq G_R = 1$ here.

Here one can observe the shortcomings in believing that bandwidth via the model Eq. (17) can securely suppress SRS growth. In this model, the introduced incoherence affects the complex phase and the amplitude, giving birth to a broad distribution of laser intensity. This wide distribution is the dominant reason that amplification produces high and undesirable values of $\bar{G}$.

2. Nonlinearity from kinetic effects

The bandwidth effects acting on the linear convective amplification of SRS have been revisited above. Typically, stage ① with 'linear' growth is attained within a sub-ps interval. It may then be followed by a second stage of development when the plasma wave level attained is high enough such that kinetic effects come into play.

We have recorded the $\langle\bar{G}\rangle$ and $\sigma(\bar{G})$ during the second growth stage from simulations at three different time instants, as reported in Table II. At the time $\sim$ 1ps, the recorded values are analogous to those found for the linear regime, suggesting that kinetic effects still have a weak impact up to this moment. One can therefore expect a similar PDF $P(\bar{G})$ as discussed above in Sec. III C 1. Nevertheless, as the amplitude of EPW continues growing in time, the nonlinear evolution gives birth to inflationary growth. Moreover, it increases the spread in the development between different realisations, such that the standard deviation $\sigma(\bar{G})$ becomes large. Both can be deduced from the PDF $P(\bar{G})$ in Fig. 10, where one recognizes, first of all, a shift of the peak of $P(\bar{G})$ towards values of $\bar{G} > G_R$, as well as a broadening ($\sim \sigma(\bar{G})$) of the PDF towards the shape of normal distribution.

TABLE II. Average amplification in terms of the effective gain $\langle\bar{G}\rangle$ and its standard deviation $\sigma(\bar{G})$ for different bandwidth values $\Delta\omega_0$, or $\gamma_0\tau_c$, for subsequently nonlinear growth. All simulation data are based on 40 realisations.

$\Delta\omega_0/\omega_0$	$(\gamma_0\tau_c)$	$\langle\bar{G}\rangle_{(1\rm ps,1.5ps,2ps)}$			$\sigma(\bar{G})_{(1\rm ps,1.5ps,2ps)}$		
0.2%	(4.0)	1.15	1.89	2.46	0.80	1.07	1.09
0.4%	(2.0)	1.31	1.75	2.48	0.83	1.01	1.02
0.8%	(1.0)	1.55	2.07	2.49	0.78	0.82	0.93
1.6%	(0.5)	1.45	1.87	2.23	0.69	0.73	0.78
2.0%	(0.4)	1.41	1.65	2.13	0.66	0.69	0.84
4.0%	(0.2)	1.17	1.43	1.66	0.62	0.66	0.64

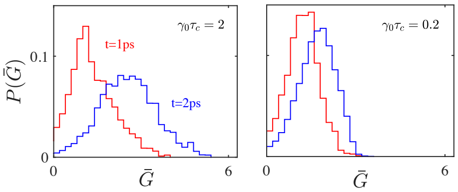

FIG. 10. $P(\bar{G})$ corresponding to $\gamma_0\tau_c = 2$ (left panel) and 0.2 (right panel) in the nonlinear growth regime. The examples illustrate that the onset of kinetic effects transform $P(\bar{G})$ into a distribution resembling a normal distribution with increasing spread in $\bar{G}$, for any $\gamma_0\tau_c$ value taken.

To well describe the nonlinear evolution as a function of the chosen bandwidth, the growth rate corresponding to $\langle\bar{G}(\Delta\omega_0)\rangle$ during this stage can be computed numerically by evaluating $\langle\bar{G}\rangle$ at time t with respect to neighboring time intervals $t + n \times dt$:

$$\gamma_k(\Delta\omega_0)|_t = \frac{\langle\bar{G}(\Delta\omega_0)\rangle|_{t+n\times dt} - \langle\bar{G}(\Delta\omega_0)\rangle|_t}{n \times dt}, \qquad (30)$$

by varying the time difference intervals in multiples of $dt = 5\gamma_0^{-1}$ (here $= 0.25$ps), namely with $n \in [1, 4]$, and for four time instants t namely $t = 1, 1.25, 1.5, 1.75$ps. In practice we determine $\sum_{j=1}^{n} j$ values, hence 10 values for $n = 4$ for each individual bandwidth value $\Delta\omega_0$ chosen.

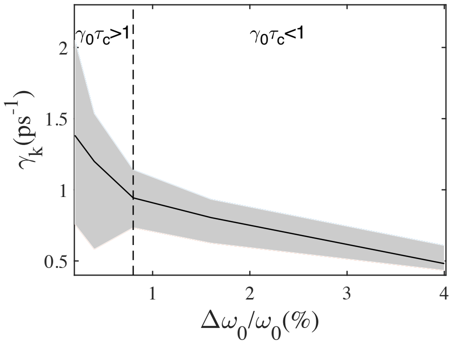

FIG. 11. The growth rate γ_k in unit of ps^{-1} according to Eq. (30) determined from numerical simulations, as a function of the relative bandwidth $\Delta\omega_0/\omega_0$ in the nonlinear regime with kinetic effects. For $\gamma_0\tau_c > 1$, the recording values of γ_k spread over a wide range, indicating the strong kinetic effects.

Visualizing these γ_k values in Fig. 11, all points fill the shaded gray area. The solid black line represents the average $\langle\gamma_k\rangle$, as a function of $\Delta\omega_0/\omega_0$, decreasing with increasing $\Delta\omega_0/\omega_0$. Notice that the γ_k values spread over a wide range (remaining well below the value of γ_0) around their average value for $\gamma_0\tau_c > 1$. This indicates their strong sensitivity to pump pulse wave trains from different realisations. The importance of kinetic effects is particularly strong at this stage and for this bandwidth regime. In contrast, for high bandwidth values with $\gamma_0\tau_c < 1$, the spread around the average value $\langle\gamma_k\rangle$ of the growth rate is strongly reduced. This suggests relatively moderate growth in this regime with a tendency towards stabilization with increasing bandwidth. For this reason we denote the regime with strong nonlinear effects for $\gamma_0\tau_c > 1$ as 'kinetic regime', while for $\gamma_0\tau_c < 1$ one can speak of a 'quasi-fluid regime'.

3. Nonlinear growth of SRS in quasi-fluid regime

In the following, we develop a semi-analytical expression for the growth rate γ_k in the quasi-fluid regime via a scaling law approach.

The 'linear' growth of SRS takes place inside the domain $[-x_l, x_l]$, where[52] $x_l = \pi\Delta\omega_0/(4v_Lk'')$, for which the spatial amplification rate is defined as $\kappa_s = G_R/(2x_l)$. The maximum mismatch coming from the density gradient is given by $v_Lk''x_I = \pi\Delta\omega_0/4$. This mismatch is considered the maximum detuning between the three waves, within which they can maintain effective interaction. However, in the nonlinear regime, the kinetic frequency shift compensates the mismatch from gradients, leading to a broader interaction domain. If we consider the maximum detuning $\pi\Delta\omega_0/4$ as unchanged, the effective interaction domain $[-x_{nl}, x_{nl}]$ is determined by $v_Lk''x_{nl} - \eta\omega_L|n_L|^{1/2} = \pi\Delta\omega_0/4$.

Combining the effective interaction domain and the linear spatial amplification rate, one can calculate the gain value over the interval, namely,

$$\bar{G} = 2x_{nl}\kappa_s = \frac{\pi\Delta\omega_0/4 + \eta\omega_L|n_L|^{1/2}}{v_Lk''x_l}G_R. \tag{31}$$

The increment $\delta G \equiv \bar{G} - G_R$ between the evolution of $\bar{G}$ with respect to G_R can be estimated using Eq.(31), and the corresponding time interval by $\delta t = (x_{nl} - x_l)/v_L = \eta\omega_L|n_L|^{1/2}/(v_L^2k'')$. The effective growth rate γ_k results in

$$\gamma_k = \frac{\delta G}{\delta t} = G_R\frac{4v_L^2k''}{\pi\Delta\omega_0} = 2(\gamma_0\tau_c)\left(\frac{v_L}{v_1}\right)\gamma_0, \tag{32}$$

and describes the growth beyond the Rosenbluth amplification, for which we have also used Eq. (10) and $\Delta\omega_0 = 2/\tau_c$. However, essential drawbacks arise from Eq. (32) since the density gradient and kinetic factor are disregarded in the above expression. The gradient length L of the plasma profile and the kinetic factor are essential to determine the nonlinear evolution. In Ref. 33 a modulation frequency is proposed that is related to the nonlinear behavior of scattered light. This frequency is proportional to the kinetic frequency shift $\delta\omega_{nl}$. We adopt a scaling law ansatz for γ_k, being a function of the modulation frequency, i.e., $\gamma_k \propto \eta|n_L|^{1/2}$, while $|n_L|^{1/2}$ is supposed to follow $|n_L|^{1/2} \propto L\eta^{-\alpha}$, with α varied between 0.41 and 0.71, calculated from Ref. 54. Hence $\gamma_k \propto L\eta^{1-\alpha}$, combined with Eq. (32) results in

$$\gamma_k = \rho\,\eta^{1-\alpha}\left(\frac{L}{100\mu m}\right)(\gamma_0\tau_c)\left(\frac{v_L}{v_1}\right)\gamma_0, \tag{33}$$

wherein α and ρ are the parameters to be adjusted.

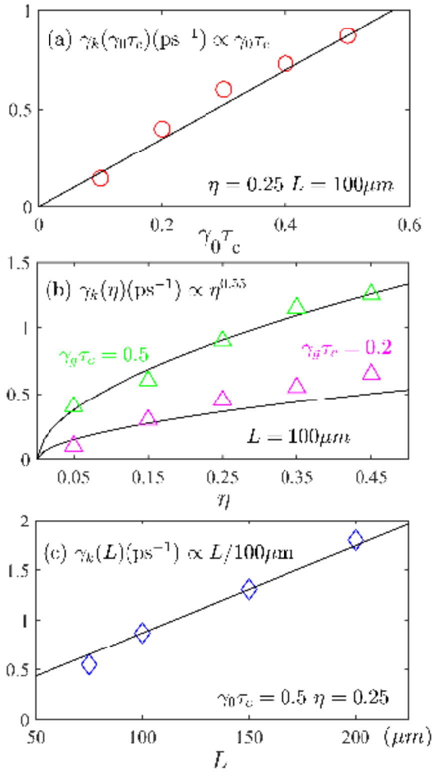

FIG. 12. Growth rate γ_k in relation to $\gamma_0\tau_c$, η and L: in (a) as a function $\gamma_0\tau_c$ for fixed values of η =0.25 and the profile gradient length L =100μm, in (b) as a function of the kinetic factor η for fixed values of $\gamma_0\tau_c$ =0.2 and 0.5 and L =100μm, and in (c) as a function of the gradient length L for fixed η =0.25 and $\gamma_0\tau_c$ =0.5. Markers in different color correspond to numerical simulations, solid lines to the parameter scaling indicated in the legend, i.e., in (a) linear with $\propto \gamma_0\tau_c$, in (b) $\propto \eta^{0.55}$, and in (c) linear in L.

Physics of Plasmas

PLEASE CITE THIS ARTICLE AS DOI: 10.1063/5.0078985

AIP Publishing

The γ_k values determined directly from the simulation results corresponding to different τ_c, η and L, are reported in Fig. 12 (colored markers). The direct fit relative to Eq. (33) gives the best agreement for the values of $\alpha = 0.45$ and $\rho = 4.4$.

Combining Eqs. (32) and (27), then the evolution of $\langle\bar{G}\rangle$ versus time can be described by

$$\langle\bar{G}\rangle = \begin{cases} (\gamma_0\tau_c)\gamma_0 t' H(t') & t' \leq \dfrac{\pi\Delta\omega_0}{2v_1 v_l k'}, \\ \zeta\ (\gamma_0\tau_c)(\dfrac{v_L}{v_1})\gamma_0 t' + G_R & t' > \dfrac{\pi\Delta\omega_0}{2v_1 v_l k'}, \end{cases} \quad (34)$$

where $\zeta \approx 4.4\eta^{0.55}(L/100\mu m)$, and where $t' = t - t_0$, t_0 is the time which scattered light takes to propagate from the interaction domain to left boundary. In Fig. 13, we show the numerically determined instantaneous values of $\langle\bar{G}\rangle$, together with the expression Eq. (34) (black dashed line). Good agreement is obtained within $\sim$ 2ps.

Underneath the concept of the "quasi-fluid" regime corresponds to moderate nonlinearity of the EPW, namely moderate kinetic effects. With increasing density gradient length, leading to a high G_R value, one can expect high amplitudes for the EPWs, such that the "quasi-fluid" of SRS can no longer exist.

IV. STATISTICAL PROPERTIES OF LASER PUMP BANDWIDTH ON SRS AMPLIFICATION

In continuation of Sec. III C 2 in which bandwidth effects on the average effective gain were considered, we investigate in this section the evolution of the distribution of gain values resulting from numerous realisations. We also take into account the nonlinear evolution of Landau damping computed using Eq. (20).

From simulation results based on PIC, as well as two-dimensional or three-dimensional fluid simulations, the relevant observables, like the backscatter level, are generally expressed via the mean value with standard deviation. The obtained values are usually based only on a few realisations due to the computational expense required to perform such simulations. Error bars to the observables are mostly rough estimates, not really based on representative statistical observation.

In contrast to PIC or multi-dimensional fluid simulations, the 3-wave coupling model allows us to establish good statistics of the SRS evolution based on a great number of realisations of the incoming pump wave signal. The flexibility of the code and the number of simulations possible to run with the 3-wave coupling model allows us to get a clear picture of the physics process of inflationary SRS.

A. Sensitivity of the growth on kinetic effects

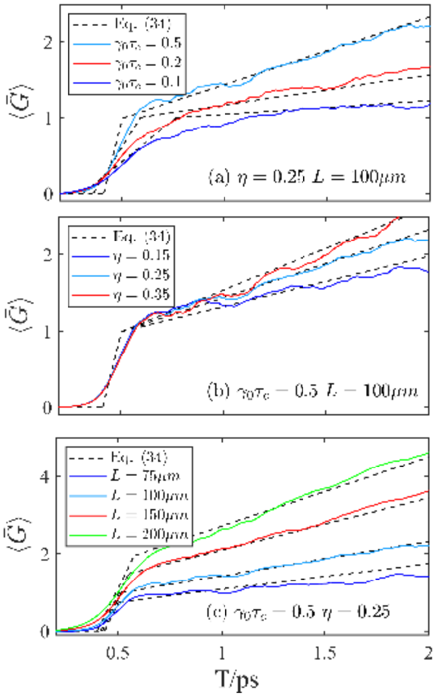

FIG. 13. Evolution of average effective gain $\langle\bar{G}\rangle$ versus time obtained from simulations: (a) for different $\gamma_0\tau_c$ values with $\eta = 0.25$ and $L = 100\mu m$; (b) For different η values with $\gamma_0\tau_c = 0.5$ and $L = 100\mu m$; (c) For characteristic length L with $\gamma_0\tau_c = 0.5$, $\eta = 0.25$. Dashed black lines indicate the values computed from the model, Eq. (34).

We have studied the sensitivity of SRS backscatter amplification on the pump intensity by varying the value of the Rosenbluth gain G_R, expected for amplification in the inhomogeneous profile. We consider the kinetic regime and examine the sensitivity of the parameters entering in the nonlinear Landau damping model of Eq. (20). Herefore, the parameter β can be adjusted to trigger the onset of nonlinear damping with plasma wave amplitude. With respect to the value recommended in Ref. 33, $\beta = 1.2$, larger (lower) values lead to a faster (slower) decrease of the damping with increasing amplitude. The comparison between the undamped and nonlinearly the damped EPWs, with the choice $\beta = 1.2$, is shown in Fig. 14. The effective gain values $\bar{G}$, have been obtained by averaging over 40 realisations with 3-wave coupling simulations, taken at time 2ps. It is remarkable that although the cases without damping and with nonlinear damping exhibit similar behavior of $\bar{G}$ for G_R >2, the onset of nonlinear growth beyond the Rosenbluth solution ($\bar{G} = G_R$, black dashed line) is prevented for the damped case in the small gain value regime G_R ≤2.

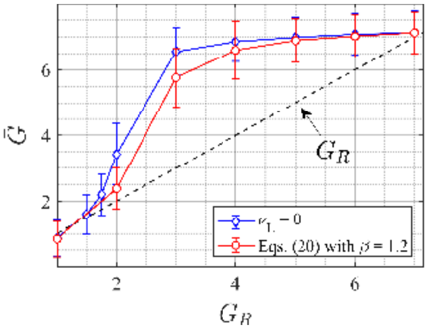

FIG. 14. Effective gain $\bar{G}$ as a function of the Rosenbluth gain G_R taken at t ≃2ps. The black dashed line corresponds to $\bar{G} = G_R$ as a guideline. The curves with markers correspond to the undamped case (blue) and the case with nonlinear Landau damping (with β =1.2), respectively. Saturation due to pump depletion is observed for G_R >3. The bandwidth chosen in the pump for all simulations here is $\Delta\omega_0 = 0$.

Fig. 14 as a guide suggests the proper choice of G_R to see the full impact of the pump laser bandwidth. For the following study we have chosen the particular value of G_R =3 with fully developed kinetic nonlinearity but not yet being in the range of strong pump depletion.

B. Bandwidth effects on the probability of further growth

To illustrate the role of bandwidth on the SRS amplification, we show in Fig. 15 results of simulations with the 3-wave coupling model. The shaded gray area as a function of the relative bandwidth $\Delta\omega_0/\omega_0$, is determined by the mean values $\langle\bar{G}\rangle$ and the standard deviation. The values are taken after 1.5ps interaction time. The results are based on 40 realisations for each bandwidth value marked. Values from single realisations of PIC simulations are also shown as $\bar{G}_{\mathrm{PIC}}$ in Fig. 15. PIC simulations start with a higher noise level, so that in particular for $\Delta\omega_0/\omega_0 < 2.8\%$ the simulations may be subject to earlier onset pump wave depletion, limiting the upper bound for $\bar{G}$. Nevertheless the PIC results fit well to the expectation values determined from the 3-wave coupling model, well-centered inside the shaded area of the confidence range. Another informative quantity is the maximum kinetic frequency shift $\delta\omega_{\mathrm{nl,m}}$, also shown in Fig. 15 via the blue curve related to right-hand-side axis. This quantity is again determined by averaging over 40 realisations. The tendency of $\langle\delta\omega_{\mathrm{nl,m}}\rangle$ as a function of $\Delta\omega_0$ coincides with the one for $\bar{G}$ from both simulation methods. The vertical blue dashed line located closely at $\Delta\omega_0/\omega_0 \approx 2.8\%$ or $\gamma_0\tau_c \approx 0.5$, separates the domain in regimes for which the ratio $\langle\delta\omega_{\mathrm{nl,m}}\rangle/\Delta\omega_0$ is smaller/larger than 1. The bandwidth value found for the above criterion is close to what was already observed

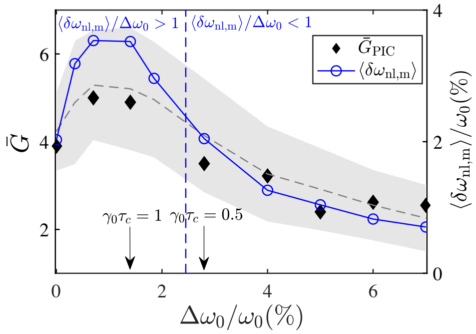

FIG. 15. SRS amplification, in terms of the effective gain value $\bar{G}$ as a function of the relative bandwidth $\Delta\omega_0/\omega_0$. The dashed line shows the expectation value $\langle\bar{G}\rangle$ obtained from 3-wave coupling simulations (40 realisations for 10 bandwidth values), taken after t =1.5ps of interaction. The shaded area indicates the interval, $\langle\bar{G}\rangle \pm \sigma(\bar{G})$ inside the standard deviation around $\langle\bar{G}\rangle$. In addition, black symbols show single realization from PIC simulations. Furthermore, the blue line with data points indicates the average maximum kinetic frequency shift $\langle\delta\omega_{\mathrm{nl,m}}\rangle$ (normalized by ω_0) from 3-wave-coupling simulations over 40 realisations (right vertical axis).

in Sec. III C 2 with G_R=1, and reflected in Table.II. It shows the effectiveness of the laser bandwidth for $\gamma_0\tau_c < 0.5$ to reduce inflationary growth of SRS by limiting the amplitude of EPWs and so the vigorous onset of kinetic effects.

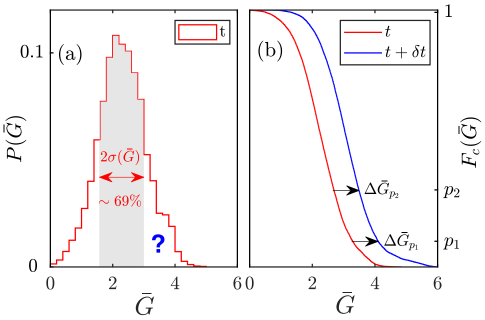

FIG. 16. (a) states that the high gain regime marked by the blue question mark, being uncovered by the mean value and error bar $\langle\bar{G}\rangle \pm \sigma(\bar{G})$, is located at the tail in the distribution $P(\bar{G})$; (b) Schematic illustration of the evolution of the distribution and $F_c(\bar{G})$ (right vertical axis) from time t to time $t + \delta t$. The increment between the G values, $\Delta\bar{G}_{p_{1,2}}$ is measured over the interval δt.

However, the criterion based on the dependence of $\langle\bar{G}\rangle \pm \sigma(\bar{G})$ and $\langle\delta\omega_{\mathrm{nl,m}}\rangle/\Delta\omega_0$ on the laser bandwidth as derived from Fig. 15, is incomplete without inspecting the distribution function $P(\bar{G})$, based on the collection of $\bar{G}$, defined in Eq. (29). This is already obvious via the width of the shaded zone shown in Fig. 15. In Fig. 16(a), we show an example of a distribution function $P(\bar{G})$ (red curve), based on the collection of $\bar{G}$, defined in Eq. (29). The confidence interval as marked by the shaded curve in Fig. 15 is also shown here with the shaded area: only 69% of the cases are located inside the interval $[\langle\bar{G}\rangle - \sigma(\bar{G}), \langle\bar{G}\rangle + \sigma(\bar{G})]$ for a gaussian-shaped distribution, and still 31% of the cases escape from this interval. This results in a non-negligible percentage (risk), say half of the remaining 31%, for undesirably high gain values. To do better, and not to ignore the important information from the tail of the distribution marked by the question mark in Fig. 16(a) for $P(\bar{G})$, we instead focus on inspecting the growth of gain values in the tail of the complementary distribution function $F_c(\bar{G})$. In Fig. 16(b), two $F_c(\bar{G})$ curves with the same bandwidth value at two time moments are sketched. Two probability values p_1 and p_2 are indicated in the vertical axis with $p_2 = F_c(\bar{G}_2) > p_1 = F_c(\bar{G}_1)$, while $\bar{G}_2 = F_c^{-1}(p_2) < \bar{G}_1 = F_c^{-1}(p_1)$. Here $F_c^{-1}(p)$ is the inverse function of $F_c(\bar{G})$.

We could imagine a long exponential tail in $F_c(\bar{G})$ for the non-well chosen bandwidth, as stated in Sec. III C 1. Its growth could be faster than that in the central part of $F_c(\bar{G})$ (where $P(\bar{G})$ is peaked). Such enhanced growth happens for a part of the realisations with high instantaneous pump laser intensities, before the pump depletion comes into play. Note that while the tail in the distribution of pump laser intensities still follows an exponential distribution, the amplification process enhances the percentage of those realisations for the scattered light. To inspect this enhancement, we compute the increments $\Delta\bar{G}_{p_1} = \bar{G}_{p_1}|_{t+\delta t} - \bar{G}_{p_1}|_t$, $\Delta\bar{G}_{p_2} = \bar{G}_{p_2}|_{t+\delta t} - \bar{G}_{p_2}|_t$, as well as $\bar{G}_{p_1}$ and $\bar{G}_{p_2}$ over a time interval δt, the result of which is sketched in Fig. 16(b). In a regime of favourable suppression of growth in the tail, the gain value $\bar{G}_{p1}$ at $p_1 < p_2$ should evolve similarly as (or slightly less than) $\bar{G}_{p2}$, while, in the opposite regime of a stronger growth rate $\Delta\bar{G}_{p_1}/\delta t$ at p_1, the risk that high gain values can occur would increase.

We have evaluated the growth rates $\Delta\bar{G}_p/\delta t$ by selecting three probability levels, namely $p = 10\%, 30\%$, and 50%, and for the bandwidth range $\Delta\omega_0/\omega_0 = 0.35\% \ldots 7\%$, corresponding to $\gamma_0\tau_c = 4 \ldots 0.2$. A procedure equivalent to Eq. (30) has been carried out, to quantify the increment of $\bar{G}_p$, or the temporal evolution of the tail in $F_c(\bar{G})$ for each bandwidth case,

$$\frac{\Delta\bar{G}_p}{\delta t} = \frac{\bar{G}_p|_{t+n\times dt} - \bar{G}_p|_t}{n \times dt}. \tag{35}$$

The same choice of time instants t and values for n and dt is taken as in Eq. (30). Again 10 values of $\Delta\bar{G}_p/\delta t$ are obtained for each individual $\Delta\omega_0$, and are recorded in Fig. 17 for the different probabilities, 50% in Fig. 17(a), 30% in Fig. 17(b), and 10% in Fig. 17(c). Fig. 17(d) shows the outer bounds of the values from(a)-(c), while Fig. 17(e) the differential spread between $\bar{G}_{30\%}$ and $\bar{G}_{50\%}$ over by G_R.

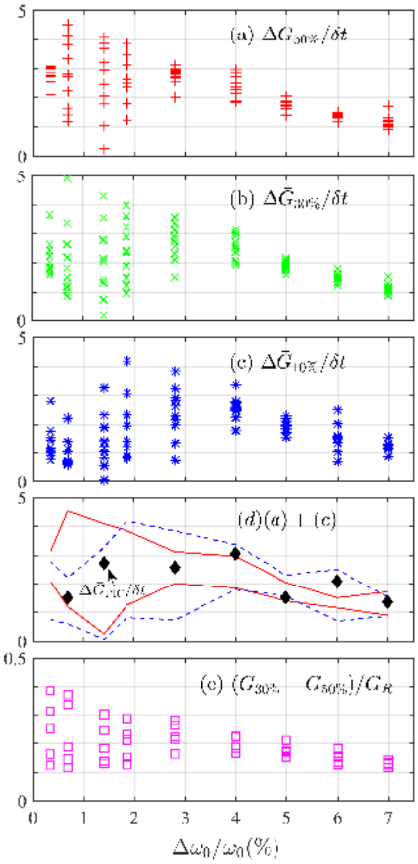

FIG. 17. Numerical evaluation of the temporal increment $\Delta\bar{G}_p/\delta t$ in units of ps^{-1} from Eq. (35) as a function of the relative bandwidth $\Delta\omega_0/\omega_0$ shown for complementary probabilities $p = F_c(\bar{G})$ at (a) $p = 50\%$, (b) $= 30\%$ and (c) $= 10\%$. For each bandwidth value, 10 simulation data points computed from Eq. (35) are shown. Subplot (d) shows the envelopes following the outermost data points from (a)-(c); indicating the value of $\Delta\bar{G}_p/\delta t$ attained with up to 10% (upper) and up to 90% (lower bound) probability, respectively. Black symbols: PIC results from single realisations. The evolution of $\Delta\bar{G}_p/\delta t$ for 30% and 50% are difficult to distinguish in subplots (a) and (b). Therefore we show in (e) the difference between $\bar{G}_{30\%}$ and $\bar{G}_{50\%}$ divided by G_R.

Based on this study, one can identify the nonlinear regime for which bandwidth is not sufficient to mitigate inflationary SRS. In such a nonlinear regime, not only

$\bar{G}_p$, but also its increment $\Delta\bar{G}_p$ over a given time interval would continue to increase, leading to large dispersion of $\Delta\bar{G}_p/\delta t$ during different time periods. This results in un-controlled growth of $\bar{G}_p$, as seen in Fig. 17(a) and (b), where the computed $\Delta\bar{G}_p/\delta t$ spread considerably for bandwidth values below $\Delta\omega_0/\omega_0 < 2.8\%$ or $\gamma_0\tau_c > 0.5$. In the opposite regime, at least for $\Delta\omega_0/\omega_0 > 4\%$ the observed values of $\Delta\bar{G}_p/\delta t$ accumulate generally in a narrower interval.

Figure 17 therefore suggest a more severe criterion than what obtained from the expectation values of $\bar{G}$ and of $\delta\omega_{\mathrm{nl,m}}$, namely that efficient mitigation of inflationary SRS via bandwidth should be operational from $\Delta\omega_0/\omega_0 = 4\%$. According to Fig. 17(c), a bandwidth of 2.8% is not broad enough to narrow the dispersion of $\Delta\bar{G}_{10\%}/\delta t$, and thus the risk of 10% of most intense cases observed in the realisations, while it would be sufficient enough when counting already 30% and 50%, i.e. $\Delta\bar{G}_{30\%}/\delta t$ and again $\Delta\bar{G}_{50\%}/\delta t$. Only when $\Delta\omega_0/\omega_0 \geq 4\%$ or $\gamma_0\tau_c \leq 0.35$, also the dispersion of $\Delta\bar{G}_{10\%}/\delta t$ is sufficiently reduced. Remarkably, also the dispersion of $\Delta\bar{G}_{50\%}/\delta t$ and $\Delta\bar{G}_{10\%}/\delta t$ converge for $\Delta\omega_0/\omega_0 \geq 4\%$ shown in Fig. 17(d), which confirms that nonlinear growth is then mitigated with a confidence of 90%. Finally, the difference between $\bar{G}_{50\%}$ and $\bar{G}_{30\%}$ in Fig. 17(e) at different time moments confirms the tendency seen in (a)-(d) via a reduced spread with increasing bandwidth. The small variation among the values from $\Delta\omega_0/\omega_0 \geq 4\%$ indicates the stable evolution of the main part in $P(\bar{G})$ or $F_c(\bar{G})$.

V. CONCLUSIONS AND DISCUSSION

In this work, the effects of temporal incoherence in pump and seed waves affecting the 3-wave coupling process of SRS have been investigated in an inhomogeneous plasma. A 3-wave coupling model is applied, in which the trapped particle effect is considered via the nonlinear frequency shift of EPWs. A natural seed noise exciting the SRS scattered light has been introduced via a boundary condition at a defined level and computed via the Langevin equation applied to a random number generator simulating white noise. For the pump wave, we have chosen a multi-band method with controlled finite bandwidth and a Lorentzian-shaped spectrum, following Ref. 20, intending to explore the efficiency to mitigate inflationary SRS, in particular the destabilisation of SRS beyond the spatial convective amplification in the inhomogeneous plasmas. Our study consists of ① spatial amplification according to Rosenbluth's work after a fast transient growth stage; ② a regime of growth of SRS beyond the Rosenbluth solution due to destabilization via kinetic effects that compensate the inhomogeneity dephasing and lead to autoresonance; ③ a stage of strong nonlinear growth beyond the upper limit of autoresonance with high amplitude plasma waves and kinetic effects leading to violent growth in SRS up to pump depletion.

It is found that a large bandwidth boundary noise itself mitigates the onset of SRS with respect to a coherent (single-frequency) seed, especially at low-intensity values of the pump laser corresponding to Rosenbluth gain factor $G_R < 2$, such that the effective gain $\bar{G}$ would not exceed G_R. For pump intensities with $G_R \geq 2$, the system is destabilized due to the presence of kinetic effects, resulting in further amplification of SRS.

The pump bandwidth effects have been investigated in exploring the statistical distributions of the amplification process in terms of probability density function (PDF) $P(\bar{G})$ for possible effective gain values $\bar{G}$ associated with the strength of SRS amplification, obtained via a great number of simulations carried out with the 3-wave coupling code. In the linear stage where the nonlinearity of EPWs is negligible, the distribution of $\bar{G}$ for low bandwidth with long coherence time $\gamma_0\tau_c > 1$ results in a primarily exponential dependence on $\bar{G}$, with a mean effective gain $\langle\bar{G}\rangle$ value close to G_R, but allowing an exponentially decreasing probability of higher amplification. For the case of a large bandwidth in the pump wave signal and short coherence time, $\gamma_0\tau_c < 1$, the distribution $P(\bar{G})$ is close to a normal distribution peaked around $\bar{G} = G_R$, decreasing in width with increasing bandwidth.

For the nonlinear stage of SRS associated with growth and increasing $\langle\bar{G}\rangle$, due to destabilization by upcoming kinetic effects, one can estimate the growth rate in the quasi-fluid regime with $\gamma_0\tau_c < 1$ via the expression Eq. (33) given by $\gamma_k = 4.4\eta^{0.55}(L/100\mu m)(\gamma_0\tau_c)(v_L/v_1)\gamma_0$. Taking for η =0.25, furthermore $v_L/v_1 \simeq$0.03…0.07 for $T_e \simeq 1keV$, $n_e/n_c \simeq$0.01…0.1, and L =100μm, the ratio between γ_k and the standard SRS growth rate assumes values in the range $\gamma_k/\gamma_0 \sim$ (0.06…0.15) $\gamma_0\tau_c$.

Besides $\langle\bar{G}\rangle$ and the corresponding standard deviation $\sigma(\bar{G})$, the established probability density function (PDF) $P(\bar{G})$ and complementary distribution function $F_c(\bar{G})$ allow us to examine the probability of spread of possible effective gain values associated with SRS amplification. This study shows that increasing bandwidth considerably narrows the spread between the observed effective gain $\bar{G}$. High effective gain values are very likely due to a large spread in $\bar{G}$, up to several times of G_R below and around $\gamma_0\tau_c = 1$, correspondingly $\Delta\omega_0/\omega_0 = 1.4\%$, such that efficient mitigation is not expected here. However, reasonable confidence can be given that SRS is mitigated for laser bandwidth values well above $\Delta\omega_0/\omega_0 \simeq 2.8\%$, corresponding to $\gamma_0\tau_c < 0.5$. With particularly high confidence, say with 90% probability excluding extreme events, nonlinear growth of SRS should be mitigated for $\Delta\omega_0/\omega_0$ >4% and $\gamma_0\tau_c < 0.35$.

For the sake of performing a significant number of realisations in order to get statistical information on the reliability of bandwidth effects, we have solved the system of partial differential in a single dimension and for relatively short plasma density profiles. We are aware that these are limitations with respect to the multi-dimensional nature of the process studied and to real-size plasmas. We use a 3-wave coupling model in which kinetic effects are described only via a phenomenological, amplitude-dependent description of the EPW, which has, of course, a limited range of validity with respect to fully kinetic simulations.

Also other parametric instabilities may appear in connection and/or in competition with SRS in the considered plasma, such as the Langmuir Decay Instability (LDI) and Stimulated Brillouin Scattering (SBS). Both LDI and SBS, not taken into account in our 3-wave model, rely on the excitation of ion acoustic waves which naturally grow on a longer (ps) time scale than Langmuir waves. LDI should not really be important in the time window we consider in this study because it is associated with important ion wave perturbations. The optimum regime of LDI[27,55] is usually expected for the criterion $k_L\lambda_D \leq 0.29$, while for the plasma considered here the values of $k_L\lambda_D$, being around 0.34, are more favourable for kinetic effects. Also, while SRS evolves vigorously within the time window of about 2ps considered in our numerical study, SBS should not become important when considering that it starts from a low natural noise level: e.g., for the reference parameter, with $v_{\rm osc}/v_{\rm th} \sim 0.2$, SBS would grow about 2 orders of magnitude per ps.

Our study focuses on the possible mitigation of SRS and the growth of Langmuir waves (EPWs) via bandwidth. In the regime that fulfills the requirement of relatively high bandwidth in the incoming laser pump according to our study, the risk of the ongoing growth of SRS backscatter is diminished and allows to control the level of SRS and of Langmuir waves. Consequently one would expect that also the levels of the potentially upcoming ion acoustic perturbations were mitigated.

In the opposite case of insufficient pump laser bandwidth, destabilizing effects due to nonlinear plasma waves will arise, and at later times one should also expect that LDI and SBS play a role. On the different time scales saturation mechanisms will also come into play. Those associated with the EPW, not considered in our model, like side-band instability as well as wave breaking should then arise and may be the leading saturation mechanisms for the growth of SRS. Some of them can help to tame and/or to saturate SRS. However, as long as pump depletion plays the decisive role for saturation, the effect on mitigation for SRS stays weak.

An equivalent study with numerous realisations using a fully kinetic code, either in one or more dimensions, is still difficult to envisage, and multi-dimensional studies with wave-coupling codes[33,56] remain computationally expensive.

The results obtained in our study are relevant for dynamics inside laser hot spots, so, e.g., of optically smoothed laser beams[57–59]. Laser hot spots usually cover a wide range of peak intensity values, corresponding in our study to the pump laser intensity, expressed via an initial value of the Rosenbluth gain G_R. Our study, due to restriction to a single spatial dimension, is focused on the mitigation capacity of the temporal aspect of optical smoothing on SRS in laser speckles[12]. Spatio-temporal smoothing methods rely on both finite bandwidth and spatial incoherence. Currently available methods at major laser facilities, such as SSD, are inefficient in controlling SRS. Better methods have to be identified, in which the interaction leading to SRS (and SBS) needs to be reduced both in time and space. Our results can therefore help to optimize coherence time parameters for smoothing methods via laser pulses composed of spike trains[16,17,19], or via "ISI"[11].

ACKNOWLEDGMENTS

The work was supported by the Strategic Priority Research Program of Chinese Academy of Sciences (Grant No. XDA25050100), the National Natural Science Foundation of China (Grant Nos. 11975154, 11675108, 11655002, 11775144), the Science Challenge Project (No. TZ2018005), and the China Scholarship Council. This work has been carried out within the framework of the EUROfusion Consortium and has received funding from the Euratom research and training programme 2014-2018 and 2019-2020 under grant agreement No 633053. The views and opinions expressed herein do not necessarily reflect those of the European Commission. We thank the CPHT computer support team.

DATA AVAILABILITY

The data that support the findings of this study are available from the corresponding author upon reasonable request.

Appendix: Generation of incoherent light signals

We derive and discuss here the procedure for generating the seed noise signal and its application to the pump wave signal with bandwidth. To generate the stochastic source term $S(t)$ concerned in the right side of Eq. (7) in practice, the Langevin equation is used:

$$\left(\frac{\partial}{\partial t} + \frac{1}{\tau_1}\right) S(t) = \frac{1}{\tau_1} Q(t), \tag{A1}$$

where the stochastic function $Q(t)$ corresponds to white noise in time, $Q(t) = |Q| \exp i\Phi(t)$, with $|Q|^2 = \Lambda$ and Φ a random phase distributed between $[-\pi, \pi)$ uniformly. The corresponding correlation function and Lorentzian power spectrum of $S(t)$ are respectively given by

$$C_1(\delta t) = \frac{\langle S(t)S^*(t+\delta t)\rangle}{\langle S(t)S^*(t)\rangle} = e^{-|\delta t|/\tau_1},\ |f(\omega)|^2 = \frac{1}{\omega^2\tau_1^2 + 1},$$

which are consistent with Eqs. (14) and (15). The coherence time τ_c for a given correlation function $C(t)$ is then defined by

$$\tau_c = \int_{-\infty}^{+\infty} dt |C(t)|^2, \tag{A2}$$

with $\tau_c = \tau_1$ for $C = C_1$. For incoherence in the pump laser field $a_0(t)$ we denote τ_c as the pump coherence time with $C_0(\delta t) = (\langle a_0^*(t)a_0(t+\delta t)\rangle)/(\langle a_0^*(t)a_0(t)\rangle) = \exp(-|\delta t|/\tau_c)$ as the corresponding correlation function. The pump correlation time is related to the laser bandwidth $\Delta\omega_0$ by $\tau_c = 2/\Delta\omega_0$. Figure 18 illustrates of the intensity spectrum $I(\delta\omega)$ following a Lorentzian shape corresponding to the spectrum used in Eq. (18) after normalization, and the corresponding correlation function $C_0(\tau)$ with 2% bandwidth. The Lorentzian envelopes from the approach via Langevin's equation (A1) is used to determine the amplitude, the 4000 discrete modes used in our simulations to generate the pump power spectrum. This spectrum is abridged when the amplitude of the spectral intensity attains 0.4% of the peak value, and its range therefore confined in between the frequencies outermost ω_1 and ω_N, here N =4000 with $\delta\omega_1 = -\delta\omega_N = |\omega_{1,N} - \omega_0|$. The choice of an abridged spectrum is preferable for reasons of numerical convergence in order to suppress undesired high frequencies $\omega_0 \pm \pi/\Delta t$ related to the choice of the time step Δt.

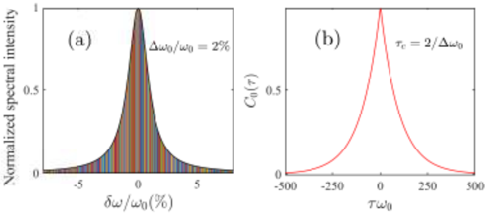

FIG. 18. (a) Intensity spectrum (normalized) with a Lorentzian shape similar to $|f|^2$ as a function of the deviation $\delta\omega$ from the central frequency ω_0 for the pump laser $I(\delta\omega)$, see Eq. (18) in the main text, and (b) the corresponding correlation function $C_0(\tau)$ having the bandwidth $\Delta\omega_0/\omega_0 = 2\%$.

REFERENCES

[1] J. J. Thomson, Phys. Fluids **17** (1974), 10.1063/1.1694940.

[2] S. Tamor, Phys. Fluids **16** (1973), 10.1063/1.1694484.

[3] E. J. Valeo and C. R. Oberman, Phys. Rev. Lett. **30**, 1035 (1973).

[4] M. N. Rosenbluth and C. S. Liu, Phys. Rev. Lett. **29**, 701 (1972).

[5] M. N. Rosenbluth, Phys. Rev. Lett. **29**, 565 (1972).

[6] J. F. Drake, Phys. Fluids **17** (1974), 10.1063/1.1694789.

[7] R. P. Drake, R. E. Turner, B. F. Lasinski, K. G. Estabrook, E. M. Campbell, C. L. Wang, D. W. Phillion, E. A. Williams, and W. L. Kruer, Phys. Rev. Lett. **53**, 1739 (1984).

[8] B. J. Winjum, J. E. Fahlen, F. S. Tsung, and W. B. Mori, Phys. Rev. Lett. **110**, 165001 (2013).

[9] Y. Kato and K. Mima, Appl. Phys. B **29**, 186 (1982).

[10] J. Garnier, Phys. Plasmas **6**, 1601 (1999).

[11] R. H. Lehmberg, A. J. Schmitt, and S. E. Bodner, J. Appl. Phys. **62**, 2680 (1987).

[12] P. Mounaix, L. Divol, S. Hüller, and V. T. Tikhonchuk, Phys. Rev. Lett. **85**, 4526 (2000).

[13] S. Skupsky, R. W. Short, T. Kessler, R. S. Craxton, S. Letzring, and J. M. Soures, J. Appl. Phys. **66**, 3456 (1989).

[14] J. E. Rothenberg, J. Opt. Soc. Am. B **14**, 1664 (1997).

[15] J. Garnier, L. Videau, C. Gouédard, and A. Migus, J. Opt. Soc. Am. A **14**, 1928 (1997).

[16] B. Afeyan and S. Hüller, Eur. Phys. J. **59**, 05009 (2013).

[17] S. Hüller and B. Afeyan, Eur. Phys. J. **59**, 05010 (2013).

[18] M. Duluc, D. Penninckx, P. Loiseau, G. Riazuelo, and E. D'humières, Phys. Rev. Appl. **12**, 054055 (2019).

[19] B. J. Albright, L. Yin, and B. Afeyan, Phys. Rev. Lett. **113**, 045002 (2014).

[20] R. K. Follett, J. G. Shaw, J. F. Myatt, C. Dorrer, D. H. Froula, and J. P. Palastro, Phys. Plasmas **26** (2019), 10.1063/1.5098479.

[21] H. Wen, R. K. Follett, A. V. Maximov, D. H. Froula, F. S. Tsung, and J. P. Palastro, Phys. Plasmas **28** (2021), 10.1063/5.0036768.

[22] T. Chapman, S. Hüller, P. E. Masson-Laborde, A. Heron, D. Pesme, and W. Rozmus, Phys. Rev. Lett. **108**, 145003 (2012).

[23] T. Chapman, S. Hüller, P. E. Masson-Laborde, W. Rozmus, and D. Pesme, Phys. Plasmas **17** (2010), 10.1063/1.3529362.

[24] H. A. Rose and D. A. Russell, Phys. Plasmas **8**, 4784 (2001).

[25] D. W. Forslund, J. M. Kindel, and E. L. Lindman, Phys. Fluids **18** (1975), 10.1063/1.861248.

[26] H. X. Vu, D. F. DuBois, and B. Bezzerides, Phys. Plasmas **9**, 1745 (2002).

[27] J. L. Kline, D. S. Montgomery, L. Yin, D. F. DuBois, B. J. Albright, B. Bezzerides, J. A. Cobble, E. S. Dodd, D. F. DuBois, J. C. Fernández, R. P. Johnson, J. M. Kindel, H. A. Rose, H. X. Vu, and W. Daughton, Phys. Plasmas **13** (2006), 10.1063/1.2178777.

[28] G. J. Morales and T. M. O'Neil, Phys. Rev. Lett. **28**, 417 (1972).

[29] R. L. Dewar, Phys. Fluids **15** (1972), 10.1063/1.1693969.

[30] L. Friedland, Phys. Rev. Lett. **69**, 1749 (1992).

[31] O. Yaakobi, L. Friedland, R. R. Lindberg, A. E. Charman, G. Penn, and J. S. Wurtele, Phys. Plasmas **15** (2008), 10.1063/1.2884717.

[32] P. Khain, L. Friedland, A. G. Shagalov, and J. S. Wurtele, Phys. Plasmas **19** (2012), 10.1063/1.4737609.

[33] G. Tran, P. Loiseau, A. Fusaro, A. Héron, S. Hüller, L. Maëder, P. E. Masson-Laborde, D. Penninckx, and G. Riazuelo, Phys. Plasmas **27** (2020), 10.1063/5.0018669.

[34] S. Ichimaru, Annals of Physics **20**, 78 (1962).

[35] W. L. Kruer, S. C. Wilks, B. B. Afeyan, and R. K. Kirkwood, Phys. Plasmas **3**, 382 (1996).

[36] H. A. Rose, Phys. Plasmas **4**, 437 (1997).

[37] D. S. Montgomery, B. B. Afeyan, J. A. Cobble, J. C. Fernández, M. D. Wilke, S. H. Glenzer, R. K. Kirkwood, B. J. MacGowan, J. D. Moody, E. L. Lindman, D. H. Munro, B. H. Wilde, H. A. Rose, D. F. Dubois, B. Bezzerides, and H. X. Vu, Phys. Plasmas **5**, 1973 (1998).

[38] S. J. Spencer, A. G. Seaton, T. Goffrey, and T. D. Arber, Phys. Plasmas **27** (2020), 10.1063/5.0022901.

[39] C. L. Tang, J. Appl. Phys. **37**, 2945 (1966).

[40] P. Mounaix, D. Pesme, and M. Casanova, Phys. Rev. E **55**, 4653 (1997).

[41] Y. Zhao, S. Weng, M. Chen, J. Zheng, H. Zhuo, C. Ren, Z. Sheng, and J. Zhang, Phys. Plasmas **24** (2017), 10.1063/1.5003420.

[42] Y. Zhao, S. Weng, Z. Sheng, and J. Zhu, Plasma Phys. Controlled Fusion **61** (2019), 10.1088/1361-6587/ab4691.

[43] R. K. Follett, J. G. Shaw, J. F. Myatt, J. P. Palastro, R. W. Short, and D. H. Froula, Phys. Rev. Lett. **120**, 135005 (2018).

[44] N. A. Yampolsky and N. J. Fisch, Phys. Plasmas **16** (2009), 10.1063/1.3160604.

[45] D. Bénisti, N. A. Yampolsky, and N. J. Fisch, Physics of Plasmas **19**, 013110 (2012), https://doi.org/10.1063/1.3677264.

[46] P. E. Masson-Laborde, W. Rozmus, Z. Peng, D. Pesme, S. Hüller, M. Casanova, V. Y. Bychenkov, T. Chapman, and P. Loiseau, Phys. Plasmas **17** (2010), 10.1063/1.3474619.

[47] E. A. Williams, B. I. Cohen, L. Divol, M. R. Dorr, J. A. Hittinger, D. E. Hinkel, A. B. Langdon, R. K. Kirkwood, D. H. Froula, and S. H. Glenzer, Phys. Plasmas **11**, 231 (2004).

[48] H. Wilhelmsson, Physica B+C **82**, 52 (1976), proceedings of the Twelfth International Conference on Phenomena in Ionized Gases.

[49] S. Hüller, P. Mulser, and A. M. Rubenchik, Phys. Fluids B **3**, 3339 (1991).

[50] P. Michel, L. Divol, D. Turnbull, and J. D. Moody, Phys. Rev. Lett. **113**, 205001 (2014).

[51] P. Michel, E. Kur, M. Lazarow, T. Chapman, L. Divol, and J. S. Wurtele, Phys. Rev. X **10** (2020), 10.1103/PhysRevX.10.021039.

[52] P. N. Guzdar, C. S. Liu, and R. H. Lehmberg, Phys. Fluids B **3**, 2882 (1991).

[53] E. Ott and T. M. Antonsen, Phys. Rev. A **39**, 3660 (1989).

[54] T. Chapman, *Autoresonance in Stimulated Raman Scattering*, Doctoral thesis, Ecole Polytechnique, Palaiseau, France (2011).

[55] J. Kline, D. Montgomery, B. Bezzerides, J. Cobble, D. DuBois, R. Johnson, H. Rose, L. Yin, and H. Vu, Physical review letters **94**, 175003 (2005).

[56] D. Bénisti, O. Morice, L. Gremillet, A. Friou, and E. Lefebvre, Phys. Plasmas **19**, 056301 (2012).

[57] D. S. Montgomery, J. D. Moody, H. A. Baldis, B. B. Afeyan, R. L. Berger, K. G. Estabrook, B. F. Lasinski, E. A. Williams, and C. Labaune, Phys. Plasmas **3**, 1728 (1996), https://doi.org/10.1063/1.871682.

[58] L. Yin, B. J. Albright, H. A. Rose, D. S. Montgomery, J. L. Kline, R. K. Kirkwood, P. Michel, K. J. Bowers, and B. Bergen, Phys. Plasmas **20**, 012702 (2013).

[59] G. Cristoforetti, S. Hüller, P. Koester, L. Antonelli, S. Atzeni, F. Baffigi, D. Batani, C. Baird, N. Booth, M. Galimberti, and et al., High Power Laser Sci. Eng. , 1–16 (2021).